

Contents lists available at ScienceDirect

Journal of the Mechanics and Physics of Solids

journal homepage: www.elsevier.com/locate/jmps



A microstructure-informed continuum model of transversely isotropic, fibre-reinforced hydrogels

Matthew G. Hennessy a , Tom Shearer b , Axel C. Moore c

- ^a School of Engineering Mathematics and Technology, University of Bristol, Bristol, UK
- ^b Department of Mathematics, University of Manchester, Manchester, UK
- ^c Department of Biomedical Engineering, Carnegie Mellon University, Pittsburgh, PA, USA

ARTICLE INFO

Keywords: Fibre-reinforced hydrogel Poroelasticity Fibre network Microstructural modelling Unconfined compression

ABSTRACT

Fibre-reinforced hydrogels are promising materials for biomedical applications due to their strength, toughness, and tunability. However, it remains unclear how to design fibre-reinforced hydrogels for use in specific applications due to the lack of a robust modelling framework that can predict and hence optimise their behaviour. In this paper, we present a microstructureinformed continuum model for transversely isotropic fibre-reinforced hydrogels that captures the specific geometry of the fibre network. The model accounts for slack (or crimp) in the initial fibre network that is gradually removed upon deformation. The mechanical model for the fibre network is coupled to a nonlinear poroelastic model for the hydrogel matrix that accounts for osmotic stress. We find that slack in the fibre network leads to J-shaped stress-strain curves, as seen in experiments, and a more isotropic swelling of the material. The model is compared to data from time-dependent unconfined compression experiments. Although we find qualitative agreement between model and experiment, the discrepancies suggest that additional physics, such as viscoelasticity and slip between the fibre network and the hydrogel matrix, can play important roles in these materials. We showcase how the model can be used to guide the design of materials for artificial cartilage by exploring how to maximise interstitial fluid pressure. Fluid pressurisation can be increased by using stiffer fibres, removing slack from the fibre network prior to matrix hydration, and reducing the Young's modulus of the hydrogel matrix. Finally, a high-level and open-source Python package has been developed for simulating unconfined compression experiments using the model.

1. Introduction

Hydrogels consist of highly hydrated networks of polymer chains, which are used in diverse applications ranging from contact lenses (Ishihara et al., 2023) to soft robotics (Chen et al., 2023). They are valued as biomaterials due to their biocompatibility (Nasra et al., 2023), biodegradability (Zhang et al., 2021), and tuneable physical properties (Smith and Senior, 2021), and are being increasingly used in regenerative medicine (Revete et al., 2022). However, hydrogels suffer from low strength and toughness owing to their high water content, and they are often unable to satisfy the mechanical demands of biomedical applications (Agrawal et al., 2013). Various approaches have been proposed to strengthen and toughen hydrogels (Fuchs et al., 2020), which include increasing the uniformity of the polymer network (Sakai et al., 2008), creating multifunctional crosslinks using nanostructure

E-mail addresses: matthew.hennessy@bristol.ac.uk (M.G. Hennessy), tom.shearer@manchester.ac.uk (T. Shearer).

https://doi.org/10.1016/j.jmps.2025.106350

Received 13 April 2025; Received in revised form 27 August 2025; Accepted 5 September 2025

Available online 15 September 2025

0022-5096/© 2025 The Authors. Published by Elsevier Ltd. This is an open access article under the CC BY license (http://creativecommons.org/licenses/by/4.0/).

^{*} Corresponding author.

¹ Equal contributions

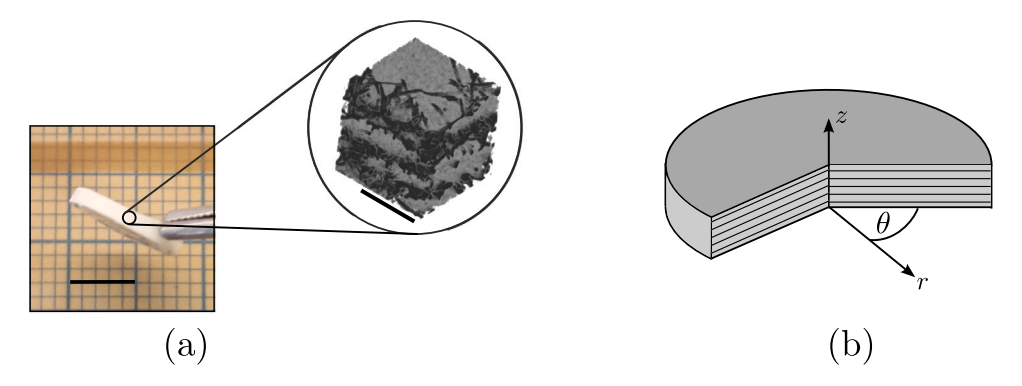


Fig. 1. (a) Photograph (scale bar = 5 mm) of a transversely isotropic fibre-reinforced hydrogel fabricated by Moore et al. (2023) along with a 3D reconstruction using nano computed tomography (scale bar = $50 \mu m$). (b) A mathematical idealisation of a transversely isotropic fibre-reinforced hydrogel, with the layers of fibre network shown as parallel black lines in the cross section.

additives (Haraguchi and Takehisa, 2002), and adding a second, interpenetrating polymer network (Dragan, 2014). Hydrogels that are reinforced by a fibre network have shown particular promise in biomedicine (Beckett et al., 2020) as the strength and toughness of the fibre network removes the need to use highly crosslinked hydrogels, which can lead to unfavourable environments for cells. In addition, fibre-reinforced hydrogels offer a great deal of tunability, as the fibre stiffness (Tan et al., 2023), volume fraction (Visser et al., 2015; Jordan et al., 2017; Moore et al., 2023), and alignment (Bas et al., 2015; Castilho et al., 2019) can all be varied to produce composite materials with optimal mechanical and poroelastic responses.

Despite the advantages of fibre-reinforced hydrogels, there remain challenges in engineering these materials for use in specific applications. In particular, there is a lack of understanding of how the fibre properties and the geometry of the fibre network should be varied in order to produce tailored macroscopic responses (Beckett et al., 2024). Mathematical and computational models of varying complexity have been used to shed light on the macroscopic response of fibre-reinforced hydrogels. The Halpin-Tsai (HT) equations (Halpin and Kardos, 1976) are a relatively simple micromechanical model that describes the stiffness of a fibre-reinforced matrix in terms of the fibre and matrix properties. Jordan et al. (2017) found that the HT equations do not always provide accurate predictions of the stiffness of fibre-reinforced hydrogels, and they attributed discrepancies to the large contrast in the Young's moduli of the fibres and the hydrogel matrix. Beckett et al. (2024) also showed that the HT equations have limited applicability to fibre-reinforced hydrogels and proposed that swelling of the hydrogel matrix could invalidate the assumptions that underpin the HT equations. Visser et al. (2015) developed a simple expression for the stiffness of transversely isotropic fibre-reinforced hydrogels in terms of the fibre properties. Subsequent studies by Castilho et al. (2019) and Chen et al. (2020) used three-dimensional (3D) finite element simulations to understand, respectively, the nonlinear elastic and linear poroelastic response of the composites produced by Visser et al. Due to the specific geometry of the fibre network used by Visser et al. in which the fibres are laid down to form a two-dimensional (2D) grid, the modelling results of Castilho, Chen, et al. might not carry over to other systems. Other authors have developed general continuum mechanics models of fibre-reinforced soft hydrated materials that account for the microstructure of the fibre network along with fluid transport (Ateshian, 2006; Ateshian et al., 2009; Safavi et al., 2023; Nian et al., 2023; Bosnjak et al., 2019; Chen et al., 2021). Simulating the models required the use of 3D finite element analysis carried out using bespoke codes or commercial software. The high computational cost of 3D finite element simulations, along with the effort required to create bespoke code, reduces their use as predictive design tools.

The purpose of this paper is, therefore, to present a flexible and computationally efficient microstructure-informed continuum modelling framework for fibre-reinforced hydrogels that is implemented in a high-level open-source Python package. The modelling framework links the fibre properties and fibre network geometry to the macroscopic material response. In contrast to previous work on modelling fibre-reinforced hydrogels (Safavi et al., 2023; Nian et al., 2023; Bosnjak et al., 2019; Chen et al., 2021), we account for slack in the fibre network that is gradually removed upon deformation. We focus on modelling a class of transversely isotropic materials developed by Moore et al. (2023) to mimic the structure and mechanics of articular cartilage. These materials consisted of horizontally aligned fibre networks layered vertically and embedded in a hydrogel matrix, as shown in Fig. 1. Similar composites have been fabricated by a number of other authors (Strange et al., 2014; Visser et al., 2015; Bas et al., 2015; Beckett et al., 2024). We develop a microstructure-informed continuum model of the hydrogel and fibre phases, explicitly modelling the hydration of the gel, before considering unconfined compression tests of the composite material. We build upon techniques used for modelling fibre networks, and incorporate them within a nonlinear poroelastic framework that accounts for osmotic effects. The poroelastic modelling of the hydrogel component of the material follows standard approaches (Hong et al., 2008; Chester and Anand, 2010); hence, the main focus of this paper is on modelling the fibre network.

There is a very large scientific literature on macroscale modelling of fibre-reinforced materials within a finite elasticity, continuum mechanics framework. Models have been published that introduce structure tensors to account for the anisotropy introduced by the presence of fibres, and potential forms for the strain energy function of such materials have been proposed phenomenologically (Federico and Herzog, 2008b; Federico and Grillo, 2012; Federico, 2015; Grillo et al., 2015; Ogden, 2015).

Many authors have used this approach in the specific context of biological tissues (e.g. Gasser et al. (2006), Federico and Gasser (2010) and Vasta et al. (2018)), and it has sometimes been used in the design of fibre-reinforced materials (Klarbring et al., 2017). A typical approach involves assigning one part of the strain energy function to the matrix and another to the fibres. For example, often a neo-Hookean model is used for the matrix, and an exponential function for the fibres (as in the HGO model Holzapfel and Ogden, 2010). When the fibres are not all co-aligned, based on principles introduced by Lanir (1983), the strain energy function will often involve an integral of the fibre strain energy density multiplied by the fibre orientation distribution function (most commonly the von Mises distribution) over all possible angles. This approach often requires numerical integration, or approximation techniques based on series expansions of the strain energy function (Hashlamoun et al., 2016), for example, rather than direct analytical evaluation of the integral. In this paper, we take a different approach by analytically evaluating the integral for the fibre phase to obtain a computationally inexpensive constitutive equation that accounts for the network structure through a fibre segment recruitment function.

Many studies have been conducted over the last several decades, producing models that have discovered key structural properties of fibre networks. Fibre networks are 3D in general, but can be modelled as 2D depending on their properties. Niskanen and Alava (1994) discovered that, at low coverage (the number of fibres that occupy a given point in the plane), the transition from 2D to asymptotically 3D behaviour depends on the product of mean coverage and length; however, at high coverage, the transition depends on the product of the fibres' flexibility and width to thickness ratio. In terms of 2D network structure, the number of fibres per unit area defines a transition: above a critical density, percolation occurs (a contiguous set of fibres spans the entire network) (Li and Zhang, 2009; Li and Östling, 2013). Percolation is required for the network to behave as a solid. Fibre network structures have been well characterised, but the focus in this paper is their mechanics. Early approaches to modelling network mechanics were based on regular or perturbed lattices (Schwartz et al., 1985), before being superseded by models in which straight fibres are laid randomly and isotropically in a 2D plane. This approach, which was developed for modelling paper and is now often called the "Mikado" model, has been used since at least the early 1990s. Aström et al. (1994) used it to predict the microscopic elastic and failure properties of high density networks and found that the effective Young's modulus of a network depends on both fibre density and length and that the stresses in the network follow an exponential distribution. This work built upon that of Cox (1952), who calculated how the stress in a matrix-embedded fibre varies along its length, and found that it can be described by a hyperbolic cosine function. However, it has been shown that the shear-lag type model used in Cox's paper does not apply to random fibre networks that are close to the percolation threshold (Räisänen et al., 1997).

More recently, it has been shown that a fibre network's elasticity is affected not only by its connectivity, but also by the strain magnitude (the "floppy-to-rigid transition") (Arzash et al., 2020; Head et al., 2003; Shivers et al., 2019), and that its deformation falls into two regimes: one dominated by fibre bending and one by fibre stretching. In the stretching regime, the network transforms in an approximately affine way, whereas in the bending regime, the deformation is distinctly non-affine (Humphries et al., 2018). The straightening and activation of fibre segments is critical to the mechanical behaviour of the network (Vainio and Paulapuro, 2005, 2007), a principle similar to the recruitment of collagen fibres in biological soft tissues (Paetsch et al., 2012; Shearer, 2015b,a; Hamedzadeh et al., 2018; Shearer et al., 2020; Gregory et al., 2021; Haughton et al., 2022). In this paper, we consider two cases: firstly we assume that the fibre segments are straight and that the network deforms affinely, then we consider the gradual recruitment of wavy fibre segments. Rather than model the fibres as discrete objects, we use a continuum approach, which allows us, conveniently, to link our microscale fibre network models to a nonlinear, macroscale framework.

The paper is organised as follows. The microstructure-informed continuum model is developed and specialised to free swelling and unconfined compression experiments in Section 2. The model is then simulated, compared to experimental data, and applied to the design of artificial cartilage in Section 3. The paper concludes in Section 4.

2. Microstructural modelling of fibre-reinforced hydrogels

The microstructure-informed continuum model is derived using the framework of non-equilibrium thermodynamics. We begin by constructing the free energy of the system, which accounts for the energy of elastic deformations and hydrating the material. The free energy is then used to derive thermodynamically consistent constitutive relations that can be used in the bulk equations. We shall consider deformations from a nominal unhydrated state to a hydrated reference state, and from the hydrated state a further deformation will be applied, as shown in Fig. 2. A table of nomenclature is provided in SM1.

2.1. Modelling of the fibrous phase of the material

We first derive two microstructure-informed constitutive models for the fibrous phase of the material. We consider a twodimensional network of fibres and assume that it deforms according to an affine mapping (an assumption that is appropriate for high-density fibre networks (Agarwal et al., 2023)). Based upon this assumption, we calculate the strain energy in an arbitrary fibre segment with a specified initial angle, and then calculate the total strain energy in the network by integrating this expression over all angles. For the first constitutive model, we assume the fibres are all initially straight; in the second, we assume that they are wavy and are gradually recruited with increasing tensile strain.

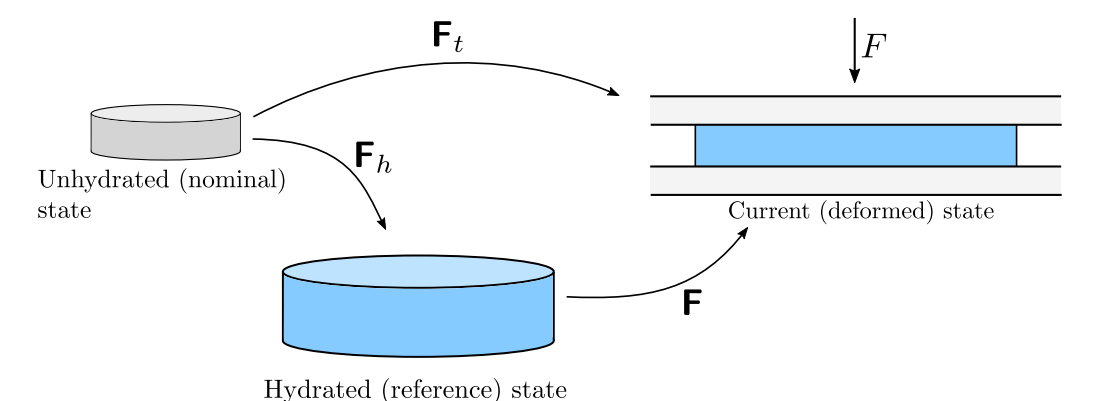


Fig. 2. The three spatial configurations used in the model and the deformation gradient tensors used to move between them. The unhydrated (nominal) state represents the material as it was prepared before hydration. The hydrated (reference) state corresponds to a freely swollen material and is used as a reference configuration to formulate the model equations. The current (deformed) state in this work corresponds to an unconfined compression experiment, where a cylindrical sample has been placed between two plattens and an axial force, *F*, has been applied.

2.1.1. The strain energy function for fibre networks with initially straight fibres

Consider a fibre segment of initial length S, that makes an initial angle $\Theta \in [0,\pi)$ with the X-axis, and is embedded in a fibre network of sufficiently high density that the network deforms in an affine manner. The fibre segment forms the hypotenuse of a right-angle triangle with initial side lengths ΔX and ΔY aligned with the X- and Y-axes, respectively. Now assume that the network is subjected to an affine deformation consisting of homogeneous stretches λ_1 and λ_2 in the X- and Y-directions, respectively (without loss of generality, we shall assume $\lambda_1 \geq \lambda_2$), so that the total deformation gradient is

$$\mathbf{F}_t = \begin{pmatrix} \lambda_1 & 0 \\ 0 & \lambda_2 \end{pmatrix}. \tag{1}$$

We define the two-dimensional invariants of the left and right Cauchy–Green deformation tensors $(\mathbf{B}_t = \mathbf{F}_t \mathbf{F}_t^T)$ and $\mathbf{C}_t = \mathbf{F}_t^T \mathbf{F}_t$, respectively) associated with this deformation as $I_1 = \operatorname{tr}(\mathbf{B}_t) = \operatorname{tr}(\mathbf{C}_t) = \lambda_1^2 + \lambda_2^2$ and $I_2 = \operatorname{det}(\mathbf{B}_t) = \operatorname{det}(\mathbf{C}_t) = \lambda_1^2 \lambda_2^2$. The fibre segment is thus deformed according to Fig. 3. The following identities clearly hold:

$$\Delta X = S \cos \Theta, \quad \Delta Y = S \sin \Theta,$$
 (2)

$$s^{2} = \Delta x^{2} + \Delta y^{2} = \lambda_{1}^{2} \Delta X^{2} + \lambda_{2}^{2} \Delta Y^{2} = S^{2} \lambda_{1}^{2} \cos^{2} \Theta + S^{2} \lambda_{2}^{2} \sin^{2} \Theta.$$
 (3)

Thus, the stretch in the fibre segment, λ , is given by

$$\lambda = \frac{s}{S} = \sqrt{\lambda_1^2 \cos^2 \Theta + \lambda_2^2 \sin^2 \Theta}.$$
 (4)

We shall assume that the constitutive behaviour of each individual fibre segment is Hookean so that its strain energy density (per unit *initial* volume) function is

$$W_f^{(i)}(\lambda) = \frac{E_f}{2}(\lambda - 1)^2,$$
 (5)

where E_f is the fibre Young's modulus. Upon substituting (4) into (5), we can write the strain energy density in the ith fibre segment as a function of the initial fibre angle:

$$W_f^{(i)}(\Theta) = \frac{E_f}{2} \left(\sqrt{\lambda_1^2 \cos^2 \Theta + \lambda_2^2 \sin^2 \Theta} - 1 \right)^2. \tag{6}$$

Note that we have considered the strain energy density so far. The strain energy stored in the ith fibre segment will be $U_f^{(i)} = V_f^{(i)}W_f^{(i)}$, where $V_f^{(i)}$ is its volume. Therefore, the total energy stored in the fibre network is given by $U_f^{\rm tot} = \sum_{i=1}^N U_f^{(i)}$, where N is the number of fibre segments in the network. This can be written as $U_f^{\rm tot} = N\bar{U}_f$, where $\bar{U}_f = \mathbb{E}[U_f^{(i)}]$ is the average amount of strain energy stored in each fibre segment, i.e. the expectation of $U_f^{(i)}$. Since $V_f^{(i)}$ and $W_f^{(i)}$ are independent random variables for the affine deformation we are considering, we can write $\bar{U}_f = \bar{V}_f \bar{W}_f$, where $\bar{V}_f = \mathbb{E}[V_f^{(i)}]$ and $\bar{W}_f = \mathbb{E}[W_f^{(i)}]$. The total volume occupied by fibres is $V_f^{\rm tot} = N\bar{V}_f$; therefore, the total energy stored in the network is $U_f^{\rm tot} = V_f^{\rm tot} \bar{W}_f$. To obtain the total strain energy density of the whole fibre network, we simply divide through by the volume of the solid in which the fibres are embedded, V_s , to give $(V_f^{\rm tot}/V_s)\bar{W}_f = \Phi_f \bar{W}_f$, where Φ_f is the volume fraction of the fibre segments that are mechanically active in the network. In the following, we shall drop the bar on \bar{W}_f for convenience.

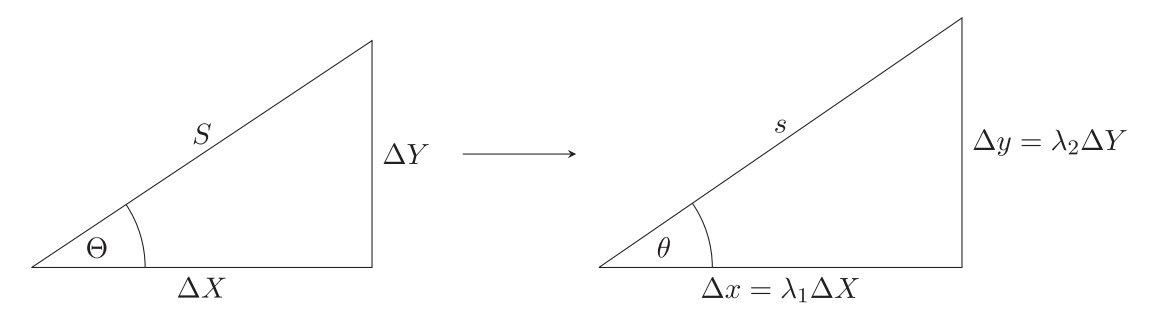


Fig. 3. The deformation of a fibre segment of initial length S and initial angle Θ .

We assume that there are so many fibres in the network that we can represent the distribution of their initial angles using a continuous probability density function. Since the fibres are isotropically oriented in the plane we shall assume a uniform probability density $U_{10,\pi^1}(\Theta)$. Therefore, the average strain energy density is

$$W_f = \int_{-\infty}^{\infty} \mathcal{U}_{[0,\pi]}(\Theta) W_f^{(i)}(\Theta) \, \mathrm{d}\Theta = \frac{1}{\pi} \int_0^{\pi} W_f^{(i)}(\Theta) \, \mathrm{d}\Theta. \tag{7}$$

Upon evaluating this integral, we obtain

$$W_f = \frac{E_f}{4} \left(\lambda_1^2 + \lambda_2^2 - \frac{8\lambda_1}{\pi} \mathcal{E} \left(1 - \frac{\lambda_2^2}{\lambda_1^2} \right) + 2 \right) \tag{8}$$

$$= \frac{E_f}{4} \left(I_1 - \frac{4\sqrt{2}}{\pi} \sqrt{I_1 + \sqrt{I_1^2 - 4I_2}} \mathcal{E} \left(2 \frac{\sqrt{I_1^2 - 4I_2}}{\sqrt{I_1^2 - 4I_2} + I_1} \right) + 2 \right), \tag{9}$$

where $\mathcal{E}(\cdot)$ is the complete elliptic integral of the second kind. Eq. (8) is only valid for $\lambda_1 \geq \lambda_2$; when $\lambda_2 > \lambda_1$, the positions of λ_1 and λ_2 in the function are swapped. In either case, the expression in terms of the invariants (9) holds. If desired, the average strain energy in the fibres, \bar{U}_f , can be calculated by multiplying this expression by \bar{V}_f .

To express this two-dimensional strain energy function in three dimensions, we assume that the layered structure of the material gives rise to transversely isotropic material behaviour, with the Z-axis being the axis of anisotropy, and we assume that λ_3 is the principal stretch in that direction. For such a material, there are five strain invariants, which can be derived by assuming that the constitutive behaviour of the material is invariant with respect to rotations around its axis of anisotropy. The following set of invariants is commonly used:

$$\hat{I}_1 = \text{tr}(\hat{\mathbf{C}}_t) = \lambda_1^2 + \lambda_2^2 + \lambda_3^2, \quad \hat{I}_2 = \frac{1}{2}(I_1^2 - \text{tr}(\hat{\mathbf{C}}_t^2)) = \lambda_1^2 \lambda_2^2 + \lambda_1^2 \lambda_3^2 + \lambda_2^2 \lambda_3^2, \tag{10}$$

$$\hat{I}_{3} = \det(\hat{\mathbf{C}}_{t}) = \lambda_{1}^{2} \lambda_{2}^{2} \lambda_{3}^{2}, \quad \hat{I}_{4} = \mathbf{M} \cdot (\hat{\mathbf{C}}_{t} \mathbf{M}) = \lambda_{3}^{2}, \quad \hat{I}_{5} = \mathbf{M} \cdot (\hat{\mathbf{C}}_{t}^{2} \mathbf{M}) = \lambda_{3}^{4}, \tag{11}$$

where $\hat{\mathbf{C}}_t = \hat{\mathbf{F}}_t^T \hat{\mathbf{F}}_t$, is the three-dimensional right Cauchy–Green deformation tensor, $\hat{\mathbf{F}}$ is the three-dimensional deformation gradient, $\mathbf{M} = E_Z$ is a unit vector pointing in the direction of the axis of anisotropy in the initial configuration, and the latter two equations make use of the assumption that the deformation gradient has no shear strains involving Z so that $\hat{F}_{13} = \hat{F}_{23} = \hat{F}_{31} = \hat{F}_{32} = 0$. Therefore, by comparing with the definitions of the 2D invariants, I_1 and I_2 , we can see that

$$I_1 = \hat{I}_1 - \hat{I}_4, \quad I_2 = \frac{\hat{I}_3}{\hat{I}_4}. \tag{12}$$

By substituting (12) into (9), a hyperelastic energy for a general three-dimensional deformation is obtained and since it depends on the deformation only via the right Cauchy–Green tensor, it is objective.

2.1.2. The strain energy function for fibre networks with initially wavy fibres

The fibre strain energy density function above was for initially straight fibre segments. Now, we will assume that the fibre segments are wavy and only resist tension once the excess length has been straightened out. We refer to the stretch required to straighten a fibre as the critical recruitment stretch. Assuming affine deformations, the critical recruitment stretch of a fibre is equal to its tortuosity.

Experiments involving fibre networks produced by electro-spinning have shown that the fibre tortuosity varies from fibre to fibre and hence can be characterised by a probability distribution (Davidson et al., 2020; Stella et al., 2010; Amajuoyi et al., 2024). Therefore, we now assume there is a distribution of waviness and we are interested in calculating the *average* strain energy density

of a fibre segment for a given waviness distribution. We characterise the waviness of an individual fibre segment in terms of its critical recruitment stretch, λ_c , and assume that its strain energy density function is

$$W_f^{(i)}(\lambda, \lambda_c) = \frac{E_f}{2} \left(\frac{\lambda}{\lambda_c} - 1\right)^2 \mathcal{H}(\lambda - \lambda_c),\tag{13}$$

where $\mathcal{H}(\cdot)$ is the Heaviside function defined as $\mathcal{H} = 0$ for $x \le 0$ and $\mathcal{H} = 1$ for x > 0. This represents a fibre that does not store any energy if the current stretch is below its recruitment stretch and is linear elastic once the stretch is above its recruitment stretch. The *average* strain energy density (averaged over the critical recruitment stretch distribution function $f(\lambda_n)$) is

$$\tilde{W}_f(\lambda) = \int_0^\infty f(\lambda_c) W_f^{(i)}(\lambda, \lambda_c) \, \mathrm{d}\lambda_c = \frac{E_f}{2} \int_0^\lambda f(\lambda_c) \left(\frac{\lambda}{\lambda_c} - 1\right)^2 \, \mathrm{d}\lambda_c. \tag{14}$$

Then, the strain energy density in the whole network (again assuming a uniform distribution of initial fibre orientations) can be written as

$$W_f = \int_{-\infty}^{\infty} \mathcal{U}_{[0,\pi]}(\Theta) \tilde{W}_f(\Theta) d\Theta = \frac{E_f}{2\pi} \int_0^{\pi} \int_0^{\lambda} f(\lambda_c) \left(\frac{\lambda}{\lambda_c} - 1\right)^2 d\lambda_c d\Theta, \tag{15}$$

where we emphasise that λ depends on the angle Θ and the principal stretches λ_1 and λ_2 through (4). The integrals in (15) can be evaluated for a given recruitment stretch distribution, $f(\lambda_c)$, and given values of the principal stretches, λ_1 and λ_2 .

A variety of recruitment stretch distributions have been experimentally measured for electro-spun fibre networks, including gamma, exponential, and linear distributions (Stella et al., 2010; Amajuoyi et al., 2024). Motivated by the experimental work of Davidson et al. (2020), we assume the recruitment stretch distribution is given by a piecewise quartic polynomial

$$f(\lambda_c) = \begin{cases} 0, & \lambda_c \le 1, \\ \frac{60\lambda_c^2(\lambda_c - 1)(\lambda_c - \lambda_m)}{3 - 5\lambda_m + 5\lambda_m^4 - 3\lambda_m^5}, & 1 \le \lambda_c \le \lambda_m, \\ 0, & \lambda_c \ge \lambda_m, \end{cases}$$
(16)

where λ_m is the maximum recruitment stretch required to engage every fibre in the network. If the recruitment stretch distribution (or, equivalently, the tortuosity distribution) has been experimentally measured, then λ_m can be obtained by fitting (16) to the data. If the recruitment stretch distribution has not been experimentally determined, then λ_m can be inferred from stress–strain measurements, as we show below. One reason we have chosen (16) for the recruitment distribution is that it allows the double integral in (15) to be calculated exactly, albeit in terms of a lengthy expression involving special functions (see SM2 for details). Moreover, the quartic distribution has only a single fitting parameter, reducing the likelihood of overfitting available data. Other distributions can be found that allow an analytical evaluation of the integral (15). The specific form of the distribution has a quantitative effect on the model predictions; however, the main qualitative features are set by the statistical properties of the distribution, such as its mode and the maximum recruitment stretch. Further details of the quartic distribution are provided in Appendix A. A comparison of three different fibre recruitment distributions can be found in Appendix B.

We find that it is sometimes more computationally efficient to use a semi-analytical approach where the inner integral in (15) is computed exactly and the outer integral is numerically approximated using the trapezoidal rule, which is exponentially accurate due to the periodicity of the integrand (Trefethen and Weideman, 2014). This hybrid approach allows a variety of fibre recruitment stretch distributions $f(\lambda_c)$ to be used in the model (e.g. uniform, normal, beta, gamma, exponential) when an exact expression for the double integral in (15) is not available. However, in the implementation discussed below, we use the piecewise quartic function defined in Eq. (16).

2.2. Combining the fibrous phase with the isotropic hydrogel matrix

In the previous section, we derived the strain energy function for the fibrous phase of the material. For the hydrogel matrix phase, we assume that the constitutive behaviour is described by an isotropic, compressible, neo-Hookean strain energy function:

$$W_m = \frac{E_m}{4(1+\nu_m)} \left(\hat{I}_1 - 3 - \log \hat{I}_3 \right) + \frac{E_m \nu_m}{(1+\nu_m)(1-2\nu_m)} \left(\sqrt{\hat{I}_3} - 1 \right)^2, \tag{17}$$

where E_m and v_m are the Young's modulus and Poisson's ratio of the matrix, respectively. The total hyperelastic strain energy function of the elastic phase is then

$$W_e(\hat{I}_1, \hat{I}_3, \hat{I}_4) = (1 - \Phi_f) W_m(\hat{I}_1, \hat{I}_3) + \Phi_f W_f(\hat{I}_1, \hat{I}_3, \hat{I}_4), \tag{18}$$

where we recall that Φ_f represents the nominal volume fraction of fibres in the non-hydrated state. From this point onward, we drop the hat notation for three-dimensional quantities, since we will no longer need to refer to the two-dimensional theory.

Now that we have derived the strain energy function for the solid phase of the material, we move on to modelling energy changes associated with its hydration.

² We use the word nominal to describe quantities in the non-hydrated configuration of the material.

2.3. Material hydration

To model the energy change of hydration, we assume the material can be treated as a single homogenised body characterised by the nominal fibre fraction Φ_f and the nominal water fraction Φ_w . The nominal water fraction measures the volume of water per unit of undeformed (non-hydrated) volume. The Flory–Huggins theory of solvent-polymer mixtures (Doi, 1996) is used to describe the energy of mixing water molecules, polymer chains, and fibre segments. The free energy density (per unit undeformed volume) is given by

$$W_{\text{mix}} = \frac{R_g T}{\Omega_w} \left[\boldsymbol{\Phi}_w \log \left(\frac{\boldsymbol{\Phi}_w}{1 + \boldsymbol{\Phi}_w} \right) + \frac{\chi(\boldsymbol{\Phi}_f) \boldsymbol{\Phi}_w}{1 + \boldsymbol{\Phi}_w} \right], \tag{19}$$

where $\Omega_w = 18 \times 10^{-6} \text{ m}^3 \text{ mol}^{-1}$ is the molar volume of water, $R_g = 8.314 \text{ J mol}^{-1} \text{ K}^{-1}$ is the universal gas constant, T = 296 K is temperature, and χ is the Flory interaction parameter, which characterises the strength of unfavourable interactions between water molecules and solid components (polymers and fibres). If $\chi \gg 1$, then it is energetically costly to hydrate the material; in this case, the amount of water uptake during the hydration phase will be small. The dependence of χ on the nominal fibre fraction Φ_f reflects the differing affinity of water to the fibre and matrix phases. Its functional form will be discussed in Section 3.1.

2.4. Balance laws and bulk equations

Having defined the free energy density of the material, $W = W_e + W_{\rm mix}$, the constitutive relations for a three-dimensional, time-dependent model can now be derived using non-equilibrium thermodynamics. For brevity, we only present the most important equations here; their derivations are provided in SM3. We choose to formulate the governing equations using a reference configuration associated with a freely swollen, hydrated state (to be determined in Section 2.5). Here, freely swollen means that there are no geometric constraints or loads applied to the material. Thus, we let the deformation gradient, \mathbf{F}_h , describe how the non-hydrated material deforms upon hydration; see Fig. 2. The relative volume change due to hydration is given by $J_h = \det \mathbf{F}_h$. We assume that the hydrogel exists in a state of full saturation upon hydration and after any load is applied. That is, the pore space is assumed to be completely occupied by fluid; there are no voids formed by air, even in the dry state. Thus, the volume of the hydrated material, V_h , is equal to the sum of the initial volume of the solid phase, V_s , and the added volume of water, V_w . Therefore, $V_h = V_s + V_w$ and $J_h = V_h/V_s = 1/(1 - \phi_0)$, where $\phi_0 = V_w/V_h$ is the initial volume fraction of water in the hydrated state. That is, ϕ_0 represents the initial porosity of the material.

Subsequent deformations relative to the hydrated state are described by the deformation gradient tensor \mathbf{F} . By introducing the displacement relative to the hydrated state, \mathbf{u} , the deformation gradient tensor can be written as $\mathbf{F} = \mathbf{I} + \nabla \mathbf{u}$, where \mathbf{I} is the identity tensor and ∇ is the gradient with respect to coordinates in the hydrated state. Similarly, $J = \det \mathbf{F}$ describes the volume of a material element in the current (deformed) state relative to its volume in the hydrated (reference) state. The total deformation gradient tensor that describes the deformation from the non-hydrated (nominal) configuration to the current (deformed) configuration is given by $\mathbf{F}_I = \mathbf{F} \mathbf{F}_I$. The total volume change of a material element relative to its volume in the non-hydrated state is $J_I = \det \mathbf{F}_I = JJ_I$.

Although the total deformation gradient tensor has been written in terms of a multiplicative decomposition, the intermediate hydrated state is not a virtual configuration as seen in models of growth, residual stress and viscoelasticity, but a true, physically realisable state (see, e.g. Moore et al. (2023)). Hence, \mathbf{F}_h , \mathbf{F}_t , and \mathbf{F}_t are true deformation gradient tensors and each deformation will be geometrically compatible.

The constituents of the material (water, polymers, fibres) are assumed to be incompressible. However, at the macroscopic level, the material can compress or expand due to local rearrangements of the polymer and fibre networks. These rearrangements are driven by the imbibition of water into, or the expulsion of water out of, material elements. Thus, the volume of a given material element is dependent on the volume of water contained within it. Since J_t describes the volume of material (water and solid components) per unit unhydrated volume, and Φ_w is the volume of water per unit unhydrated volume, we can write $J_t = 1 + \Phi_w$, a condition known as the molecular incompressibility condition. By introducing the referential water fraction $\phi_w = \Phi_w/J_h$, which measures the volume of water per unit reference volume (the volume of the initial hydrated state), the incompressibility condition can be expressed as

$$J = 1 + \phi_w - \phi_0. \tag{20}$$

The current volume fraction of water (volume of water per unit current volume, also known as the porosity) is defined as $\phi = \phi_w/J$. Conservation of mass in the water phase implies that the referential fraction of water, ϕ_w , evolves according to

$$\frac{\partial \phi_w}{\partial t} + \nabla \cdot \mathbf{Q}_w = 0, \tag{21}$$

where t is time and Q_w is the referential volumetric flux of water (volume of water per unit time per unit area of the hydrated state). The flux of water is given by a Lagrangian form of Darcy's law,

$$\mathbf{Q}_{w} = -\mathbf{J}\mathbf{F}^{-1}\mathbf{K}\mathbf{F}^{-T}\nabla p,\tag{22}$$

where K is permeability tensor of the current configuration and p is the water pressure. In a fibre-reinforced porous material, the orientation of the fibres relative to the flow can strongly impact the local permeability, and the permeability tensors derived by Federico and Herzog (2008b,a) can be used in (22).

Conservation of linear momentum, neglecting inertial terms, leads to

$$\nabla \cdot \mathbf{S} = \mathbf{0}. \tag{23}$$

where **S** is the referential stress tensor, which measures forces per unit initial area of the hydrated state. The total stress tensor is the sum of the elastic stress S^e , the osmotic stress Π , and the fluid pressure p, such that

$$S = S^{e} - [\Pi(\phi_{w}) + p]JF^{-T}.$$
(24)

The elastic component of the referential stress tensor is given by

$$\mathbf{S}^{e} = \frac{1}{J_{h}} \frac{\partial W_{e}}{\partial \mathbf{F}_{e}} \mathbf{F}_{h}^{T},\tag{25}$$

where the strain energy density W_e is given by (18) and $\left(\frac{\partial}{\partial \mathbf{A}}\right)_{ij} = \frac{\partial}{\partial A_{ij}}$ for any second-order tensor \mathbf{A} . In the absence of any deformation from the initial, hydrated state, so that $\mathbf{F} = \mathbf{I}$ and J = 1, the tensor \mathbf{S} gives the *Cauchy* stress in the initial, hydrated state. The osmotic stress is derived from the Flory–Huggins mixing energy (19) and given by

$$\Pi(\phi_w) = -\frac{\partial W_{\text{mix}}}{\partial \Phi_f} = -\frac{R_g T}{\Omega_w} \left[\log \left(\frac{\phi_w}{J} \right) + 1 - \frac{\phi_w}{J} + \chi(\Phi_f) \left(1 - \frac{\phi_w}{J} \right)^2 \right]. \tag{26}$$
 The initial condition for this system of equations is that the referential water fraction ϕ_w is equal to the porosity of the initially

The initial condition for this system of equations is that the referential water fraction ϕ_w is equal to the porosity of the initially hydrated state, ϕ_0 . The boundary conditions to be imposed are specific to the problem being considered and will be discussed in the context of free swelling and unconfined compression experiments in Sections 2.5 and 2.6 below.

2.5. Calculation of the hydrated state

Now that we have derived our governing equations, we explicitly calculate the freely swollen states that are achieved upon hydration of the non-hydrated material. For this, we envision that the material has been submersed in a bath of water. Equilibrium will be reached when the total stress S and the fluid stress (pressure) p within the composite balance the pressure of the surrounding fluid, which can be set to zero without loss of generality. Therefore, upon full hydration, the total stress and the fluid pressure within the gel will be zero, S = 0 and p = 0. Using the expression for S given by (24), these equations can be combined into

$$S^e = \Pi(\phi_0)I, \tag{27}$$

where we have used $\mathbf{F} = \mathbf{I}$ for the hydrated state and we recall from Section 2.4 that $\phi_0 = 1 - 1/J_h$ is the volume fraction of fluid in the initial hydrated state. Eq. (27) implies that in a free-swelling scenario, the elastic and osmotic stresses must balance. Moreover, since $\Pi(\phi_0) > 0$, it follows that the osmotic stress is tensile and acts to stretch the material.

We assume that the hydration of the sample leads to anisotropic, but homogeneous swelling of the solid phase with corresponding deformation gradient

$$\mathbf{F}_{h} = \begin{pmatrix} \alpha_{\parallel} & 0 & 0 \\ 0 & \alpha_{\parallel} & 0 \\ 0 & 0 & \alpha_{\perp} \end{pmatrix} \quad \Rightarrow \quad J_{h} = \alpha_{\parallel}^{2} \alpha_{\perp}, \tag{28}$$

where α_{\parallel} and α_{\perp} are stretches in the direction parallel and perpendicular to the plane of the fibres, respectively. The form of (28) leads to an elastic stress tensor of the form

$$\mathbf{S}^{e} = \begin{pmatrix} \sigma_{\parallel}^{e}(\alpha_{\parallel}, \alpha_{\perp}) & 0 & 0\\ 0 & \sigma_{\parallel}^{e}(\alpha_{\parallel}, \alpha_{\perp}) & 0\\ 0 & 0 & \sigma_{\perp}^{e}(\alpha_{\parallel}, \alpha_{\perp}) \end{pmatrix},\tag{29}$$

with σ_{\parallel}^e and σ_{\perp}^e denoting the in-plane and out-of-plane Cauchy stresses of the hydrated state, which are calculated in Appendix C and are given by (C.2)–(C.5). For a given value of the Flory interaction parameter, χ , Eqs. (27)–(28) and provide three independent equations for the three unknowns: α_{\parallel} , α_{\perp} , and J_h . Alternatively, given an experimentally observed value of J_h , these three equations determine α_{\parallel} , α_{\perp} , and χ .

2.6. Specialisation to unconfined compression

The model is specialised to unconfined compression experiments by considering a cylindrical sample of hydrated material of initial radius R, height H, and porosity ϕ_0 . The sample is subjected to a compression along its longitudinal axis by placing it between two impermeable plates, which are then compressed via an imposed displacement or force F, as shown in Fig. 2. In this experiment, the sample is surrounded by water to prevent dry out. During compression, the sample is free to expand in the radial direction. The plates are assumed to be frictionless so that the cylindrical shape of the sample is preserved during compression. Thus, the height of the sample decreases to h(t) and its radius increases to $r_c(t)$. The deformation gradient then takes the form

$$\mathbf{F} = \begin{pmatrix} \beta_r(r,t) & 0 & 0 \\ 0 & \beta_{\theta}(r,t) & 0 \\ 0 & 0 & \beta_z(t) \end{pmatrix} \Rightarrow J(r,t) = \beta_r(r,t)\beta_{\theta}(r,t)\beta_z(t), \tag{30}$$

where β_r , β_θ , and β_z are the principal stretches in the radial, circumferential, and axial direction, respectively. The coordinate r measures radial distances in the initially hydrated state; thus, $0 \le r \le R$. The total stretches, measured relative to the undeformed (non-hydrated) state are given by $\lambda_r = \alpha_{\parallel}\beta_r$, $\lambda_{\theta} = \alpha_{\parallel}\beta_{\theta}$, and $\lambda_z = \alpha_{\perp}\beta_z$. The principal (referential) stresses are given by $S_i = S_i^c - [\Pi(\phi_w) + p]\beta_i^{-1}J$ with

$$S_r^e = \frac{\alpha_{\parallel}}{J_h} \frac{\partial W_e}{\partial \lambda_r}, \quad S_{\theta}^e = \frac{\alpha_{\parallel}}{J_h} \frac{\partial W_e}{\partial \lambda_{\theta}}, \quad S_z^e = \frac{\alpha_{\perp}}{J_h} \frac{\partial W_e}{\partial \lambda_z}. \tag{31}$$

In (31), the derivatives of W_e are evaluated at $\lambda_r = \alpha_{\parallel} \beta_r$, $\lambda_{\theta} = \alpha_{\parallel} \beta_{\theta}$, and $\lambda_z = \alpha_{\parallel} \beta_z$.

The axial compression of the material is assumed to induce a purely radial fluid flow. In addition, the fluid pressure is assumed to be axisymmetric and uniform along the out-of-plane (vertical) direction; thus, the pressure will only depend on the radial coordinate r and time t. Consequently, only the radial component of the permeability tensor K is required in Darcy's law (22). We denote the radial component of the permeability tensor as k and use the Holmes–Mow permeability equation (Holmes and Mow, 1990) given by

$$k(J) = k_0 \left(\frac{J - \phi_0}{1 - \phi_0}\right)^{\gamma} \exp\left[\frac{M}{2}(J^2 - 1)\right],$$
 (32)

where k_0 is the permeability of the hydrated material and γ and M are fitting parameters.

In light of the form of the deformation gradient tensor in (30), we introduce the radial displacement $u_r(r,t)$. The principal stretches can then be defined as $\beta_r = 1 + \partial u_r/\partial r$, $\beta_\theta = 1 + u_r/r$, and $\beta_z(t) = h(t)/H$. The referential fluid fraction then takes the form $\phi_w(r,t)$ and can be obtained from $\phi_w = \phi_0 + \beta_r \beta_\theta \beta_z - 1$. Under these assumptions, the balance laws representing mass and momentum conservation can be reduced to (see SM4 for details)

$$\frac{r}{2}\frac{\partial}{\partial t}\left(\beta_{\theta}^{2}\beta_{z}\right) = \frac{k(J)J}{\beta_{z}^{2}}\frac{\partial p}{\partial r},\tag{33a}$$

$$\frac{r}{2}\frac{\partial}{\partial t}\left(\beta_{\theta}^{2}\beta_{z}\right) = \frac{k(J)}{\beta_{r}}\left[\frac{\partial S_{r}^{e}}{\partial r} + \frac{S_{r}^{e} - S_{\theta}^{e}}{r} - \beta_{\theta}\beta_{z}\frac{\partial\Pi}{\partial r}\right].$$
(33b)

The mass balance (33a) determines the fluid pressure p and must be solved with the boundary condition p(R,t)=0, reflecting the continuity of fluid stress at the free boundary of the sample. The momentum balance (33b) determines the radial displacement u_r and must be solved with the boundary conditions $u_r(0,t)=0$ and $S_r(R,t)=0$. The former represents symmetry at the origin and the latter represents continuity of total stress at the free boundary. The initial conditions for (33b) are given by $u_r(r,0)=0$ and $\beta_z(0)=1$.

In a force-controlled experiment, the axial stretch β , is determined from an axial force balance given by

$$F = 2\pi \int_{0}^{R} \left[S_{z}^{e} - (\Pi + p)\beta_{r}\beta_{\theta} \right] r \, \mathrm{d}r, \tag{34}$$

where F is the applied force. We use the convention that F < 0 corresponds to axial compression. In this case, (33)–(34) must be simultaneously solved. Once the displacement is found, the radial and circumferential stretches, along with the porosity, can be computed.

In a displacement-controlled experiment, the axial stretch $\beta_z(t)$ is prescribed. In this case, the equation for the displacement (33b) decouples and can be solved independently from the rest of the equations. Once the displacement is known, the pressure p can be computed by integrating (33a). The force on the platten can be obtained by evaluating (34).

2.6.1. Equilibrium response

The equilibrium response of the material to a load is found by setting the time derivatives to zero and seeking a homogeneous deformation with $\beta_{\theta} = \beta_{r}$. The balance of fluid pressure results in p=0 everywhere. The referential water fraction can be written in terms of the stretches β_{r} and β_{z} as $\phi_{w} = \beta_{r}^{2}\beta_{z} - 1 + \phi_{0}$. For displacement-controlled loading where β_{z} is known, the radial stretch β_{r} is found by solving $S_{r}^{e} - \beta_{r}\beta_{z}\Pi(\phi_{w}) = 0$. For force-controlled loading, the radial and axial stretches must be found by simultaneously solving $S_{r}^{e} - \beta_{r}\beta_{z}\Pi(\phi_{w}) = 0$ and $F = \pi R^{2}[S_{z}^{e} - \beta_{r}^{2}\Pi(\phi_{w})]$.

2.6.2. Instantaneous response

The instantaneous response can be derived by assuming that no fluid is expelled $(\phi_w = \phi_0)$ on short time scales and that the sample remains homogeneous with $\beta_\theta = \beta_r = \beta_z^{-1/2}$. The fluid in the gel becomes pressurised with a uniform pressure P > 0 that exceeds the pressure of the surrounding fluid. The balance of total stress at the side of the sample leads to $P = \beta_z^{-1/2} S_r^e - \Pi(\phi_0)$. If β_z and hence β_r and β_θ are known due to displacement-controlled loading, then the fluid pressure P can be calculated. However, if β_z is unknown due to the loading being controlled by force, then the force balance $F = \pi R^2 (S_z^e - \beta_z^{-3/2} S_r^e)$ must first be solved.

2.7. Numerical approach

The open-source Python package ucompress.py has been developed to provide high-level, user-friendly code for simulating the hydration and unconfined compression of nonlinear poroelastic materials using the models developed here. The governing equations are discretised in space using a Chebyshev spectral method and in time using a fully implicit Euler scheme with an analytical Jacobian matrix. The package, along with tutorials, is available at https://github.com/hennessymatt/ucompress.py.

2.8. Material specification and parameter values

We consider materials that are based on the fibre-reinforced hydrogels fabricated by Moore et al. (2023) by electrohydrodynamic deposition (electrospinning and electrospraying). The authors referred to their materials as 'FiHy' (which stands for Fibre Reinforced Hydrated Network). The hydrogel matrix of FiHy is composed of gelatin ($E_m=4~\mathrm{kPa},~\nu_m=0,~\rho_m=1.2~\mathrm{g~cm^{-3}}$). The fibres are composed of polycaprolactone (PCL) ($E_f=400~\mathrm{MPa},~\rho_f=1.1~\mathrm{g~cm^{-3}}$). These parameters values are obtained from Moore et al. (2023), ChemicalBook (2025) and Beckett et al. (2024). The orientation of fibres was measured using nanoCT and found to obey a uniform distribution in the plane of isotropy, as assumed in (7). The nominal fibre fractions ranged from 0.25 to 0.76 by mass. The nominal fibre fraction by volume is calculated to range from $\Phi_f=0.26$ to 0.77. The FiHy samples were hydrated for 24 h with 1X phosphate buffered saline (PBS), which has a density that is approximately equal to that of water ($\rho_w=1~\mathrm{g~cm^{-3}}$). After hydration, the samples were approximately 80% water by mass, regardless of the fibre fraction. The volume fraction of water in the hydrated state can be calculated as $\phi_0 \simeq 0.82$ for all fibre fractions.

3. Results and discussion

3.1. Hydration of PCL-reinforced gelatin

The model is first used to study the hydration of transversely isotropic fibre-reinforced hydrogels. We first fix the nominal volume fraction of fibres to $\Phi_f = 0.26$ and vary the Flory interaction parameter χ . We consider fibre networks that are initially fully engaged with $\lambda_m = 1$ and partially engaged with $\lambda_m = 3$ (recall that λ_m is the maximum recruitment stretch in the distribution function (16)). In both cases, the deformation due to hydration is strongly anisotropic, with the radial stretch being much smaller than the axial stretch; see Fig. 4(a)-(b). The anisotropic swelling is caused by the large contrast between the Young's moduli of the fibres and the matrix. As the Flory interaction parameter increases, the radial and axial stretches decrease because the volume of water absorbed by the matrix decreases, which is reflected in the porosity of the hydrated state strongly decreasing with χ (Fig. 4(c)). Moreover, with increasing χ , it becomes less energetically favourable to swell the network and hence the osmotic stress decreases (Fig. 4(d)). In the case of a fully engaged fibre network ($\lambda_m = 1$), there is virtually no in-plane expansion of the material and all of the deformation is perpendicular to the plane of the fibres. The small in-plane deformation is expected because the osmotic stress responsible for hydration, $\Pi \sim 10$ kPa, is much smaller than the in-plane Young's modulus, which is dominated by the fibre modulus $E_f \sim 400$ MPa. Conversely, the out-of-plane Young's modulus is controlled by the gelatin matrix, $E_m \sim 4 \text{ kPa}$, and is comparable to the osmotic stress; hence, there is a substantial out-of-plane deformation. When the fibre network is only partially engaged ($\lambda_m = 3$), we see there is a larger in-plane deformation, which is due to initially inactive fibres causing a reduction in the in-plane stiffness of the material, and a smaller out-of-plane deformation. However, the in-plane stretching caused by hydration is always less than the maximum recruitment stretch. Therefore, hydration is not sufficient to fully engage the fibre network. Remarkably, the out-of-plane deformation decreases in such a way that the porosity of the material remains approximately the same in both cases. Thus, the degree of hydration is not significantly impacted by the initial level of fibre engagement.

To study how material hydration depends on the nominal fibre fraction, a model for the Flory interaction parameter χ in (19) is required. The experiments of Moore et al. (2023) showed that after 24 h of hydration, the materials had a porosity of $\phi_0 \simeq 0.82$ across a range of nominal fibre volume fractions ($\Phi_f = 0.26$ to 0.77). These findings suggest that the presence of fibres does not strongly impact the Flory interaction parameter. Thus, we set χ to a constant given by $\chi = 0.57$, which is determined by reading off the value of χ in Fig. 4(c) that leads to a porosity of $\phi_0 = 0.82$.

By fixing $\chi=0.57$ and considering fibre networks that are initially fully engaged ($\lambda_m=1$), we see that the deformation and porosity do not strongly depend on the nominal fibre fraction (Fig. 4(e)–(g)). The osmotic stress decreases linearly with Φ_f (Fig. 4(h)), reflecting the balance between osmotic stress and the out-of-plane elastic stress produced by the gelatin matrix, the latter of which is proportional to $1-\Phi_f$; see Appendix C. When initially inactive fibres are accounted for ($\lambda_m=3$), hydration leads to greater in-plane stretching and reduced out-of-plane stretching compared to the active case (as is the case when these parameters are plotted as a function of χ). Moreover, both the in-plane and out-of-plane stretches now strongly depend on the fibre fraction Φ_f . The dependence of the stretches on Φ_f ultimately results from the in-plane softening that occurs due to inactive fibres. This softening allows the osmotic stress to drive a greater in-plane expansion of the material. As the nominal fibre fraction increases, the in-plane stiffness increases as well, reducing the in-plane deformation and increasing the out-of-plane deformation. Again, whether the fibres are initially active or inactive does not greatly affect the porosity as a function of Φ_f (Fig. 4(g)).

3.2. Model comparison to unconfined compression experiments

The microstructure-informed continuum model is now compared with data produced from unconfined compression experiments carried out by Moore et al. (2023). Recall that the parameter values associated with these materials are provided in Section 2.8. Using the initial porosity of the material after hydration ($\phi_0 = 0.82$), the Flory interaction parameter has been calculated by solving the hydration equations presented in Section 2.5; we find that $\chi = 0.57$ for all samples.

The microstructure-informed continuum model is first compared with stress–strain data produced by subjecting cylindrical FiHy samples with different nominal fibre fractions ϕ_f to compressive axial loads. For each fibre fraction, ϕ_f , two different samples were fabricated and tested, resulting in two sets of stress–strain data for a given fibre fraction, ϕ_f . The short duration of the loading, which was on the order of 10 s, is much smaller than the poroelastic time scale over which fluid is squeezed out of the sample (on the

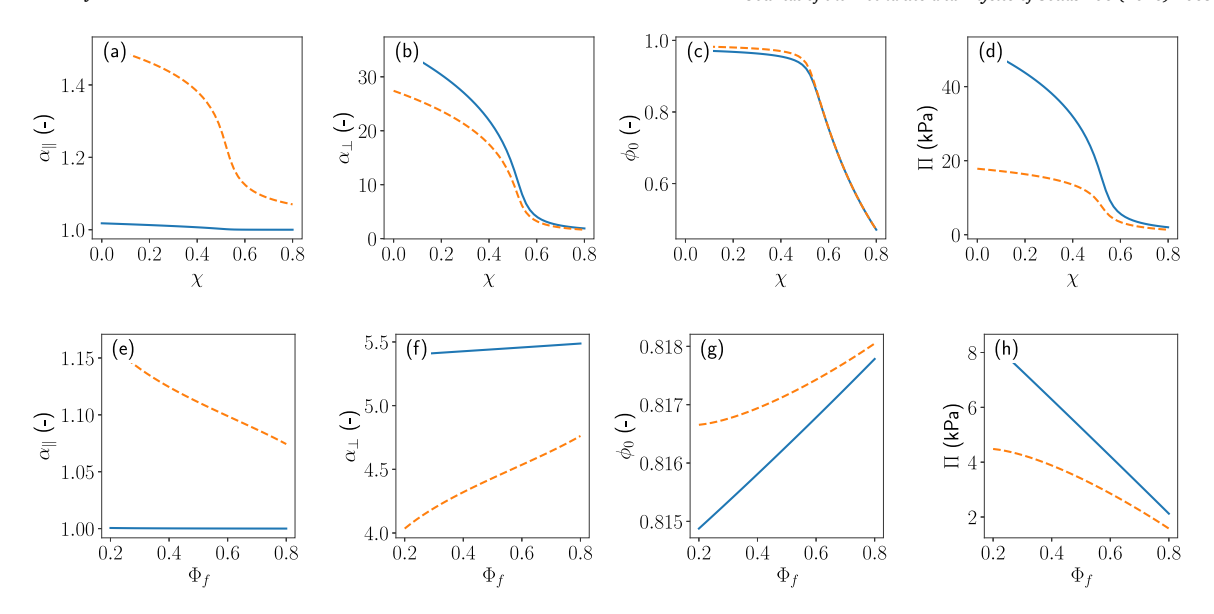


Fig. 4. Hydration of fibre-reinforced hydrogels without ($\lambda_m = 1$, solid lines) and with ($\lambda_m = 3$, dashed lines) fibre recruitment. The panels show the in-plane stretch (a, e), out-of-plane stretch (b, f), porosity of the hydrated state (c, g), and the osmotic stress (d, h) as a function of the Flory interaction parameter, χ , with $\Phi_f = 0.26$ (a–d), and the nominal fibre fraction, Φ_f , with $\chi = 0.57$ (e–h).

order of 1000 s). Hence, the stress–strain data is assumed to represent the instantaneous response of the material. The stress–strain curves exhibit the characteristic 'J' shape seen in other fibre-reinforced hydrogels (Visser et al., 2015; Beckett et al., 2020; Gloria et al., 2007; Jordan et al., 2017), whereby a large initial strain is required before any substantial increase in stress occurs (Fig. 5).

The stress–strain data can be modelled by considering a range of compressive axial stretches $\beta_z \leq 1$, corresponding to compressive axial strains of $\epsilon_z = 1 - \beta_z$, and computing the axial stress, S_z , following the procedure outlined in Section 2.6.2. If all fibres in the network are assumed to be mechanically active (no recruitment; $\lambda_m = 1$), then there are no free parameters in the model. However, the predicted stresses greatly exceed those measured in experiments; see the dashed lines in Fig. 5. This is a strong indication that, despite the materials being pre-loaded due to hydration, some mechanically inactive fibres remain in the network. By accounting for inactive fibres in the model and fitting the maximum recruitment stretch λ_m to experimental data, excellent agreement is obtained. The quartic fibre recruitment distribution, which has a mode at $\lambda_c > 1$, ensures that a finite tensile strain is needed to engage a large proportion of the fibres and induce a stress (see Appendix B for more details), which results in J-shaped stress–strain curves. When fitting λ_m , only one data set for a given fibre fraction is used, yet the model is able to capture both data sets reasonably well. The value of λ_m obtained by fitting varies with the nominal fibre fraction Φ_f . We find that for $\Phi_f = 0.26$, 0.42, 0.51 and 0.77, the best-fitting maximum recruitment stretch is $\lambda_m = 3.0$, 1.8, 1.7, and 3.9, respectively. The non-monotonic relationship between the maximum recruitment stretch and fibre fraction is evident in Fig. 5; the samples with $\Phi_f = 0.42$ and 0.51 exhibit a much more rapid increase in stress with strain, characteristic of a stiffer material caused by more fibre engagement. However, given the small number of samples produced and tested, alongside the variability of the electrohydrodynamic fabrication process, the non-monotonic relationship between the maximum recruitment stretch and the fibre fraction may not be a true characteristic of the system.

For the remainder of this section, we focus on FiHy materials that have a nominal fibre fraction $\Phi_f = 0.42$, as these were subjected to additional experimental testing. By taking the maximum recruitment stretch to be $\lambda_m = 1.8$, in line with Fig. 5(b), the mechanical properties of the material are fully characterised. The only remaining fitting parameters are related to the permeability and only influence the time-dependent solutions of the model. After hydration, the radius and height of the sample were R = 5.165 mm and H = 1.740 mm, respectively.

The instantaneous and equilibrium response of a FiHy material to different compressive loads was measured. Specifically, the axial stretch β_z was measured as a function of the applied compressive force F. The data is shown in Fig. 6. The model overestimates the magnitude of the instantaneous deformation, but underestimates the equilibrium deformation. The latter suggests there is a long-term softening mechanism at play. One explanation is that we underestimated the initial degree of hydration. From the equilibrium analysis in Section 2.6.1, we see that the applied axial load is balanced by the axial elastic stress and the osmotic stress. Since the osmotic stress decreases with fluid volume fraction, materials with increased hydration will experience greater axial deformation upon application of a force. Indeed, by setting $\chi = 0.41$ to increase the fluid fraction of the initial hydrated state to $\phi_0 = 0.97$, keeping all other parameters fixed, a much better agreement between the theoretical and experimental equilibrium response is obtained (the dashed–dotted lines in Fig. 6(b)). However, this artificial softening also impacts the instantaneous response, which the model now predicts less well. Thus, it is more likely that an alternative and overlooked physical mechanism is responsible for the discrepancy between model predictions and experiments. Candidates include solid-phase viscoelasticity, which is expected for fibre-reinforced

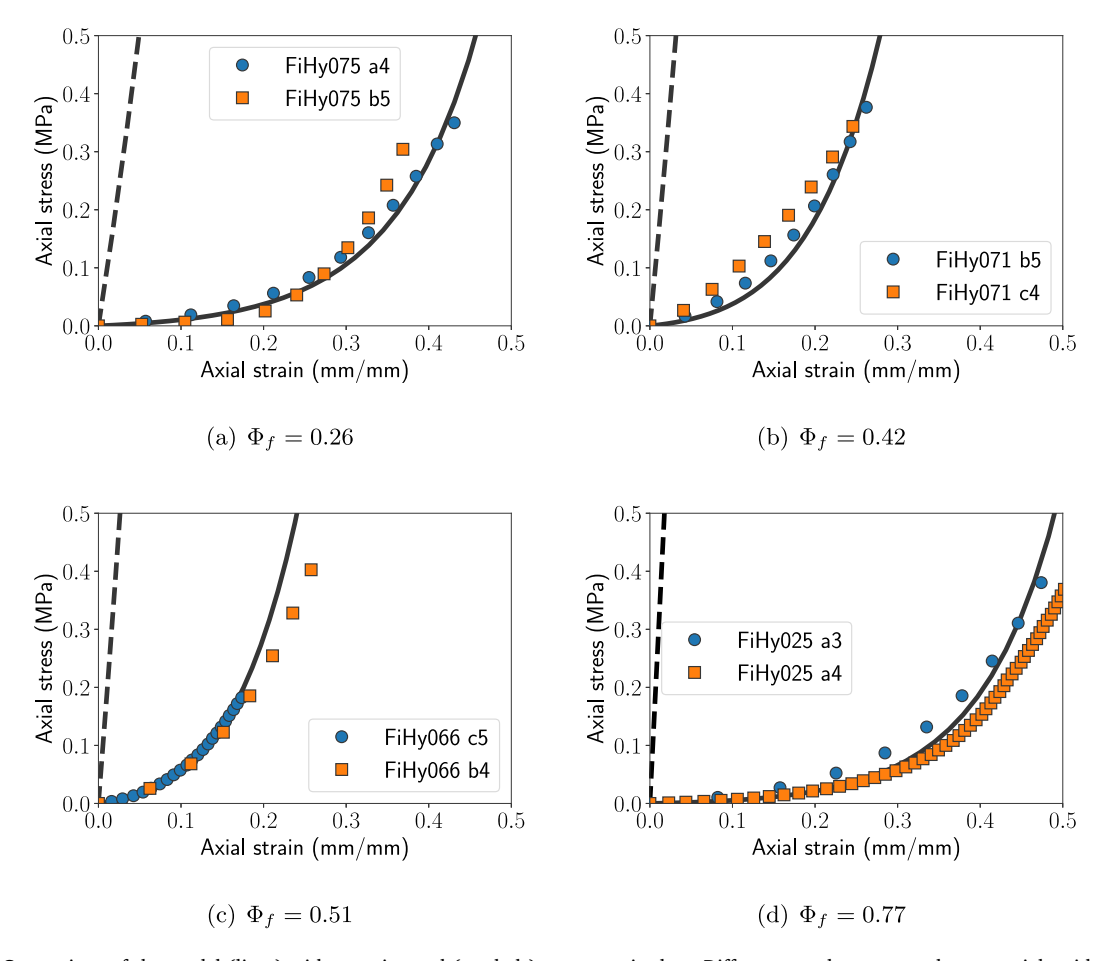


Fig. 5. Comparison of the model (lines) with experimental (symbols) stress–strain data. Different panels correspond to materials with different nominal fibre fractions Φ_f . Solid lines correspond to models that account for fibre recruitment; dashed lines correspond to models without recruitment. The maximum recruitment stretch λ_m for each panel is different; see text for details. Positive axial strains in these figures correspond to compressions rather than stretches.

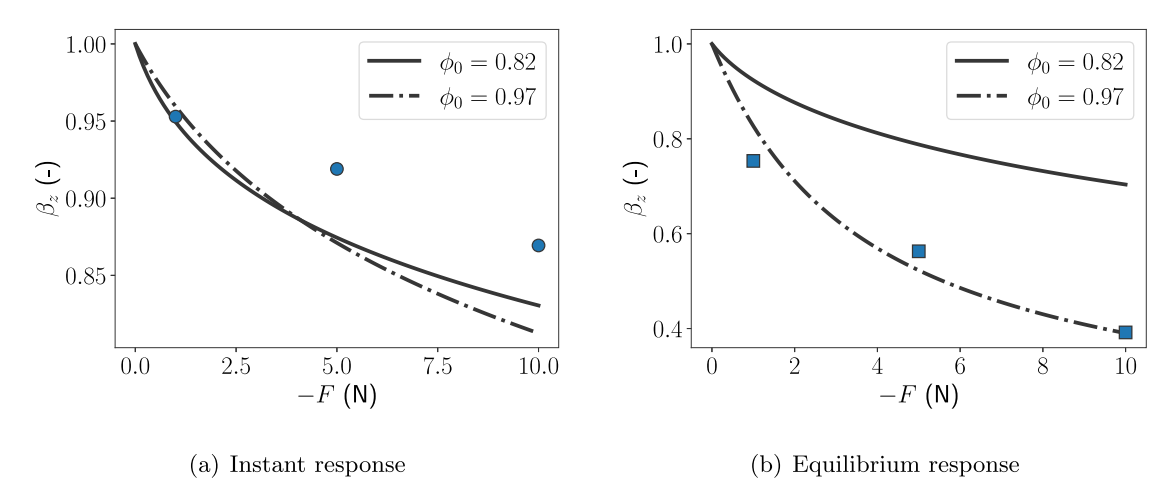


Fig. 6. Comparison of model predictions (lines) and experimental measurements (symbols) of the (a) instantaneous and (b) equilibrium response of a fibre-reinforced hydrogel to an applied force. We plot the axial stretch β_z as a function of the applied force F. Two values of the initial porosity ϕ_0 are considered.

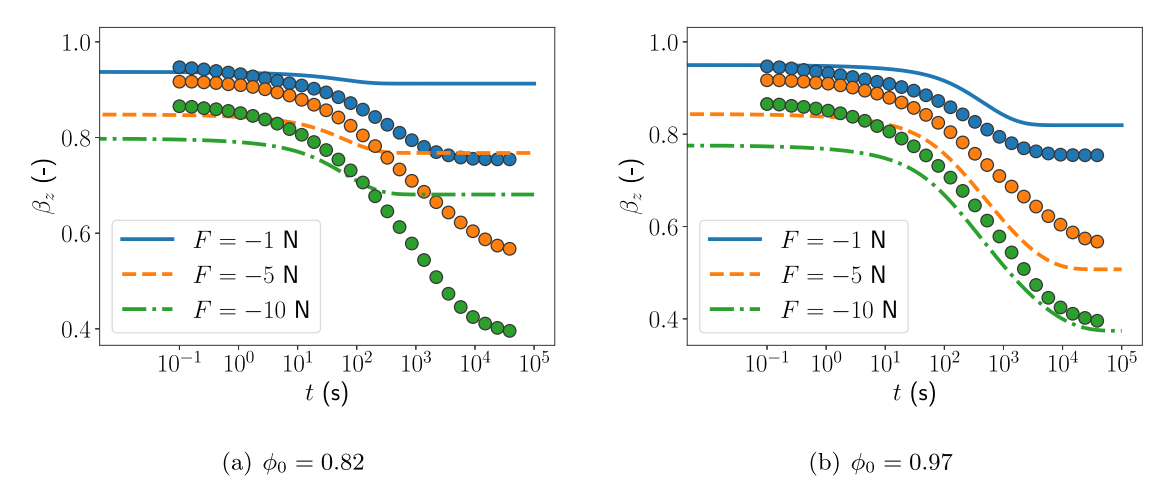


Fig. 7. Comparison of model predictions (lines) and experimental measurements (symbols) of the transient response of a fibre-reinforced hydrogel to different applied forces F. The time dependence of the axial stretch β_r is shown for two different values of the initial porosity ϕ_0 .

hydrogels (Strange et al., 2014), and slip between the fibre network and the hydrogel matrix, neither of which are considered in the model here.

The time-dependent response of a FiHy material to an axial compressive force was also studied by Moore et al. (2023). In particular, the axial stretch β_z was measured as a function of time for three applied loads, F. For small times, there are plateaus in the data that coincide with the instantaneous response of the material described in Section 2.6.2 (see Fig. 7(a)). However, a plateau in the data for large times is only seen when the applied load is small (F = -1 N), providing further evidence that the material exhibits slow viscoelastic creep.

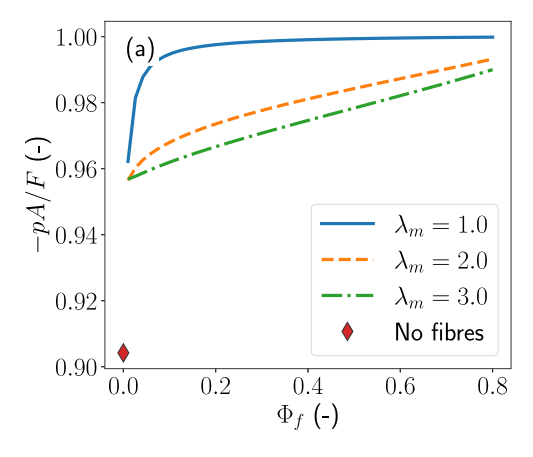
To simulate the time-dependent material response, we set the parameters in the Mow–Holmes permeability law (32) to be $k_0 = 2 \times 10^{-13}$ m² Pa⁻¹ s⁻¹, $\gamma = 4$, and M = 2. The model predictions (the solid lines in Fig. 7(a)) capture the qualitative features of the data. However, large quantitative discrepancies occur; this is mainly due to the inability of the model to capture the instantaneous and equilibrium responses of the material shown in Fig. 6. Changes to the permeability-related parameters do not strongly impact the agreement between model and experiment, as variations in k_0 only horizontally shift the model curves, whereas variations in α and M alter the transition between the instantaneous and equilibrium plateaus. However, by increasing the initial porosity to $\phi_0 = 0.97$, the time-dependent response predicted by the model is in much better agreement with the experimental data (Fig. 7(b)). These results underscore the importance of accurately modelling the instantaneous and equilibrium response of the material, which may require incorporating additional physics into the model. Nevertheless, with only a minimal number of fitting parameters, the microstructure-informed continuum model is able to capture all of the experimental data qualitatively, and, in some cases, provide excellent quantitative agreement as well.

3.3. Design of materials for artificial cartilage

Having validated our model, we now showcase how it can be used to guide the design of fibre-reinforced hydrogels used as artificial cartilage. One of the most remarkable features of cartilage is that it is able to bear compressive loads that greatly exceed its equilibrium compressive modulus (Moore et al., 2023). This load-bearing capacity occurs through the ability of cartilage to transfer load from its porous, solid matrix to the fluid residing in the pore space. Unconfined compression experiments have shown that the fraction of load supported by the interstitial fluid (also called the fluid load fraction) can be as high as 79% in human cartilage, and 94% in bovine cartilage (Park et al., 2003). Thus, any synthetic material used to replace cartilage should achieve similar fluid load fractions.

The goal of this section is to use our model to predict, understand, and optimise the fluid load fraction in transversely isotropic fibre-reinforced hydrogels during force-controlled unconfined compression. We consider cylindrical gelatin-PCL composites based on the FiHy materials produced by Moore et al. (2023) using the parameters in Section 2.8. The radius and height of the hydrated sample are taken to be R = 5.165 mm and H = 1.740 mm, respectively; the Flory interaction parameter is set to $\chi = 0.57$. The axial compressive force is set to F = -10 N.

We focus on the peak fluid load fraction, which can be obtained by solving for the instantaneous response of a sample when a compressive load is applied. On larger time scales, the fluid load fraction decays to zero due to the fluid within the sample reaching equilibrium with the external fluid; see Section 2.6.1 and Tan et al. (2023) and Moore et al. (2023). From Section 2.6.2, the instantaneous fluid pressure is given by $p = \beta_z^{-1/2} S_r^e - II$. The fluid load fraction can then be defined as -pA/F, where $A = \pi \beta_r^2 R^2$ is the current area of the circular face of the sample. Thus, the fluid load fraction is controlled by two competing mechanisms. Firstly, the radial elastic stresses act to pressurise the fluid. Secondly, the tensile osmotic stress, which resists axial compression, acts to



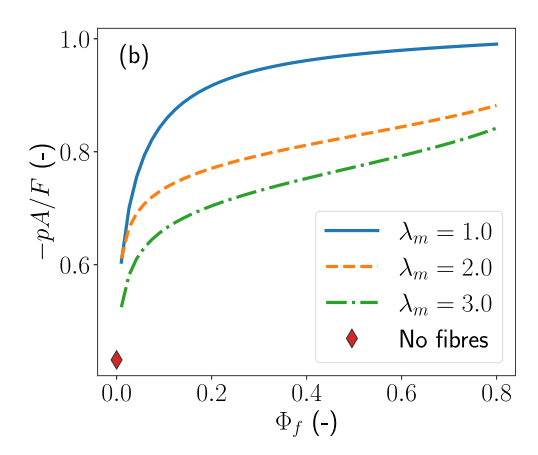


Fig. 8. Fraction of the load supported by the fluid pressure (fluid load fraction) as a function of the nominal fibre fraction Φ_f for various maximum recruitment stretches λ_m . The Young's modulus of the hydrogel matrix is (a) 4 kPa and (b) 400 kPa. The curves are computed by solving for the instantaneous response of the sample to a 10 N compressive axial force. The quantity $A = \pi R^2 \beta_r^2$ is the current area of the circular face on which the axial force is applied.

depressurise the fluid. Thus, maximising the fluid load fraction amounts to decreasing the osmotic stress and increasing the radial elastic stress.

During the instantaneous response, the amount of fluid contained within the material is fixed. As a result, the osmotic stress is equal to that of the initially hydrated state. The osmotic stress of the initially hydrated state must balance the axial elastic stress (see Section 2.5). Hence, the osmotic stress scales roughly with the Young's modulus of the hydrogel matrix and the nominal volume fraction of the matrix, $1-\Phi_f$, so that $\Pi \sim (1-\Phi_f)E_m$. Increasing the nominal fibre fraction, Φ_f , is expected to decrease the osmotic stress and increase the peak fluid load fraction, as confirmed by numerical results, which show the fluid load fraction exceeding 95%; see Fig. 8(a). The large fluid load fraction across the entire range of fibre fractions suggests that osmotic stresses only support a small fraction of the load. Indeed, the above scaling analysis shows that the osmotic stress is roughly $\Pi \sim 1$ kPa in magnitude, whereas the compressive stress induced by the load is on the order of $F/(\pi R^2) \sim 100$ kPa. Increasing the hydrogel modulus by a factor of 100 to $E_m = 400$ kPa results in greatly increased osmotic stresses and markedly lower peak fluid load fractions (Fig. 8(b)).

The radial elastic stress also plays a key role in controlling the peak fluid load fraction, and is dependent on both the Young's modulus of the fibres and the maximum recruitment stretch, λ_m . The impact of the fibre modulus on fluid load fraction has been studied by Tan et al. (2023); thus, we focus on the role of fibre engagement. As the maximum recruitment stretch increases, there are more inactive fibres in the network and the radial stiffness decreases. As a result, the fluid becomes less pressurised due to the applied force and the fluid load fraction decreases, as can be seen in Fig. 8. As an extreme case, we have computed the instantaneous response of a fibre-free network. The lack of any radial reinforcement leads to a marked decrease in the fluid load fraction; see the red diamonds in Fig. 8. Thus, radial reinforcement plays an important role in generating interstitial fluid pressure.

Moore et al. (2023) inferred the peak fluid load fraction of FiHy samples from unconfined compression experiments. They found that the fluid load fraction varied non-monotonically with the nominal fibre fraction. Generally, the fluid load fraction was maximised when the (target) ratio of gelatin to PCL was 2:1 by mass. Smaller or larger proportions of gelatin led to a decrease in the fluid load fraction. The results in Fig. 8 indicate that the fluid load fraction is sensitive to the amount of slack in the fibre network, with the fluid load fraction increasing with decreasing slack (or values of λ_m). When fitting the stress–strain data in Fig. 5, we found that materials with intermediate fibre fractions had the least amount of slack and, therefore, would be expected to have the greatest fluid load fractions, which matches with the findings of Moore et al. Thus, the maximum in the fluid load fraction observed by Moore et al. is likely due to variation in the amount of slack in the fibre network across the samples.

The degree of swelling plays an important role in controlling the fluid load fraction. We now fix the nominal fibre fraction to $\Phi_f = 0.42$ and the maximum recruitment stretch to $\lambda_m = 2$, and we vary the initial degree of hydration, J_h , which is equivalent to varying the Flory parameter χ (see Section 2.5). We consider three different values of the Young's modulus of the matrix E_m . Increasing the initial swelling ratio J_h generally leads to a reduction in the fluid load fraction (Fig. 9(a)), which we attribute to the increase in osmotic stress with J_h . Although increasing the swelling ratio also increases the proportion of fibres that are engaged after hydration (Fig. 9(b)), the increase in osmotic stress that acts to stretch the fibre network also acts against the applied load and hence decreases the fluid load fraction. Thus, swelling controls the fluid load fraction through the osmotic stress rather than by engaging fibres in the network.

3.3.1. Design implications

Our analysis of the peak fluid load fraction suggests that the load-bearing capacity of the fluid can be enhanced by decreasing the ratio of the axial stiffness to the radial stiffness. Decreasing the axial stiffness by using a softer hydrogel matrix or a greater volume fraction of fibres will decrease the osmotic stresses, allowing the fluid to bear more of the applied load. The radial stiffness can be

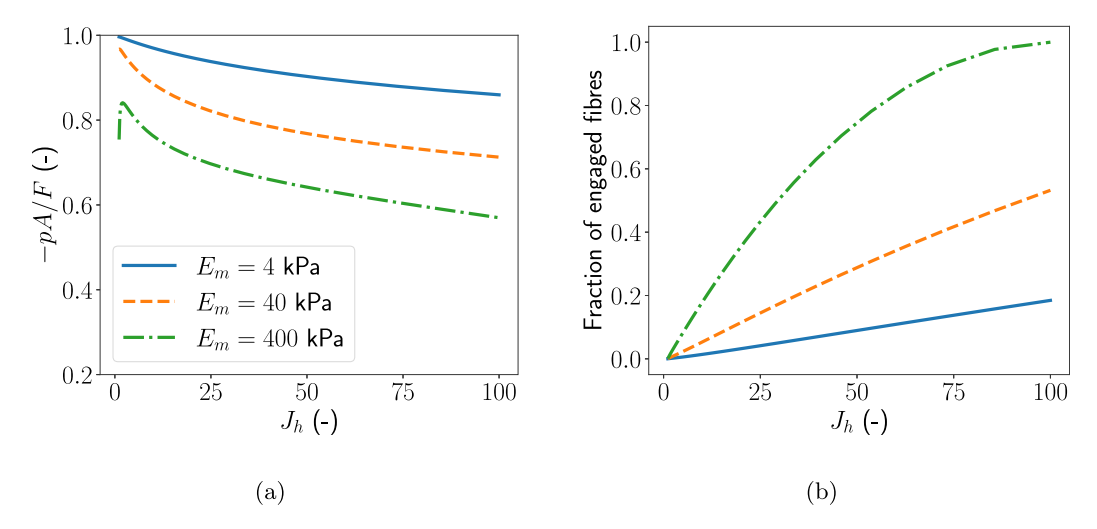


Fig. 9. (a) Fluid load fraction as a function of the initial swelling ratio J_h for different values of the Young's modulus of the matrix E_m . The applied force is F = -10 N. (b) The fraction of fibres that are engaged by matrix hydration as a function of initial swelling ratio. The legend applies to both panels.

increased by introducing a reinforcing fibrous network or increasing the fibre stiffness. The fluid load fraction can also be increased by reducing the slack in the fibre network. However, fibre slack must be removed during material fabrication and, importantly, prior to matrix hydration. Removing fibre slack after fabrication by swelling the matrix will increase the osmotic stress and reduce the fluid load fraction.

4. Conclusion

In this paper, we developed a mathematical framework for modelling fibre-reinforced hydrogel composite materials subjected to finite deformations. In particular, we derived a microstructure-informed continuum model of the fibre phase, incorporating the gradual recruitment of fibre segments due to fibre waviness, and upscaled it to a nonlinear elastic framework. This was combined with a poroelastic model of the hydrogel phase, which allowed us to model the swelling of the gel during hydration explicitly, before considering subsequent loading. The model could be equally applied to manufactured biomaterials, or collagen-based biological tissues, such as articular cartilage.

Due to the simplicity of our modelling framework compared to other multi-scale approaches for fibre-reinforced hydrogels (Castilho et al., 2019; Chen et al., 2020), it is possible to quickly sweep through parameter space to determine how changes to the material properties impact the poromechanical response of the composite. This feature allows the model to serve as a useful tool for guiding the design of new materials, which we showcased in the context of fabricating artificial cartilage. Although we considered fibre-reinforced materials that are transversely isotropic, it is possible to extend the model to more general orthotropic materials, such as those used by Visser et al. (2015) and Bas et al. (2015), by using an appropriate probability density function for the orientation of fibres in (7) or (15). Thus, our framework opens the door to optimising the fibre network geometry for specific applications.

The model is based on several key assumptions, namely affine deformations and perfect adhesion between the fibres and the hydrogel matrix. Non-affine deformations are expected to reduce the stiffness of the material by introducing gradual recruitment of fibre segments due to local microstructural rotations of the material occurring prior to local stretching. The impact on the stressstrain curve would be to amplify the 'J' shape in a manner that is analogous to increasing the maximum recruitment stretch λ_m in the current model. For the same reasons, non-affine deformations are expected to reduce the fluid load fraction. The loss of adhesion between the fibres and the hydrogel matrix would impact the stress-strain response and fluid load fraction in non-trivial ways. For instance, slip between the fibres and matrix would increase the amount of matrix deformation needed to remove slack from the fibres and thus would be analogous to increasing λ_m . However, any slip that occurs on longer time scales, such as after all the fibres are engaged, would likely be the result of the fibres relaxing to a less tensile state or not deforming further, corresponding to a loss of reinforcement and a softening of the material. This could manifest in the stress-strain curve as strain-softening or viscoelastic behaviour. Addressing these model limitations should be addressed in future work. Despite these assumptions, the model is able to capture several key features of fibre-reinforced hydrogels that have been observed experimentally. In particular, the gradual recruitment of fibres allows accurate quantitative agreement with the nonlinear, J-shaped loading curves seen in Fig. 5, as well as qualitative agreement with the time-dependent behaviour displayed in Fig. 7. To improve the quantitative agreement with the transient behaviour, it will likely be necessary to incorporate constitutive viscoelasticity into the fibres themselves. Several non-linear viscoelastic phenomena can be explained by the gradual recruitment of viscoelastic fibres (Shearer et al., 2020).

Finally, the fibres in our model are assumed to be infinitely flexible, with no bending stiffness. A potential further improvement could be to incorporate the influence of the fibres' aspect ratio on their bending stiffness into the model and investigate the corresponding mechanical effects on the network. However, it may be challenging to scale such a model up analytically to the macroscale as we have done here; thus, as always, there is a balance to be struck between the accuracy and the tractability of future models.

CRediT authorship contribution statement

Matthew G. Hennessy: Writing – review & editing, Writing – original draft, Visualization, Software, Methodology, Investigation, Conceptualization. **Tom Shearer:** Writing – review & editing, Writing – original draft, Methodology, Investigation, Formal analysis, Conceptualization. **Axel C. Moore:** Writing – review & editing, Writing – original draft, Methodology, Data curation.

Declaration of competing interest

The authors declare that they have no known competing financial interests or personal relationships that could have appeared to influence the work reported in this paper.

Appendix A. The quartic distribution function

In this paper, a piecewise quartic polynomial given by

$$f(\lambda_c) = \begin{cases} 0, & \lambda_c \le 1, \\ \frac{60\lambda_c^2(\lambda_c - 1)(\lambda_c - \lambda_m)}{3 - 5\lambda_m + 5\lambda_m^4 - 3\lambda_m^5}, & 1 \le \lambda_c \le \lambda_m, \\ 0, & \lambda_c \ge \lambda_m, \end{cases}$$
(A.1)

is used to describe the distribution of recruitment stretches λ_c required to engage the fibres in the network. Here, λ_m is the maximum recruitment stretch, which describes the stretch required to engage all of the fibres in the network. The quartic function (A.1) is a probability density function as it satisfies $\int_0^\infty f(\lambda_c) d\lambda_c = 1$. It also ensures that no fibres are pre-loaded in the reference configuration as the minimum recruitment stretch is $\lambda_c = 1$. This quartic distribution is plotted in Fig. 10(a).

Upon evaluating Eq. (14) using the quartic distribution (A.1), we find that the stretch-averaged strain energy of the fibres is

$$\tilde{W}_{f}(\lambda) = \begin{cases}
0, & \lambda \leq 1, \\
\frac{E_{f}(\lambda - 1)^{4}(5\lambda_{m} - 3 - 2\lambda)}{2(\lambda_{m} - 1)^{3}(3 + 4\lambda_{m} + 3\lambda_{m}^{2})}, & 1 \leq \lambda \leq \lambda_{m}, \\
\frac{E_{f}}{2} + \frac{5E_{f}\lambda(\lambda - \lambda_{m} - 1)}{(3 + 4\lambda_{m} + 3\lambda_{m}^{2})}, & \lambda \geq \lambda_{m},
\end{cases}$$
(A.2)

which gives rise to an average fibre segment stress ($\tilde{\sigma}_f = \mathrm{d} \tilde{W}_f/\mathrm{d} \lambda$) of

$$\tilde{\sigma}_{f}(\lambda) = \begin{cases} 0, & \lambda \leq 1, \\ \frac{5E_{f}(\lambda - 1)^{3}(2\lambda_{m} - 1 - \lambda)}{(\lambda_{m} - 1)^{3}(3 + 4\lambda_{m} + 3\lambda_{m}^{2})}, & 1 \leq \lambda \leq \lambda_{m}, \\ \frac{5E_{f}(2\lambda - \lambda_{m} - 1)}{(3 + 4\lambda_{m} + 3\lambda_{m}^{2})}, & \lambda \geq \lambda_{m}. \end{cases}$$
(A.3)

These functions are plotted in Fig. 10(b) and (c).

Appendix B. Comparison of fibre recruitment distributions

In addition to the quartic function (A.1) used to describe the distribution of fibre recruitment stretches, we also consider triangular and linear distributions. The triangular distribution is given by

$$f(\lambda_c) = \begin{cases} 0, & \lambda_c < \lambda_a, \\ \frac{2(\lambda_c - \lambda_a)}{(\lambda_m - \lambda_a)(\lambda_* - \lambda_a)}, & \lambda_a \le \lambda_c < \lambda_*, \\ \frac{2(\lambda_m - \lambda_c)}{(\lambda_m - \lambda_a)(\lambda_m - \lambda_*)}, & \lambda_* \le \lambda_c < \lambda_m, \\ 0 & \lambda_c \ge \lambda_m, \end{cases}$$
(B.1)

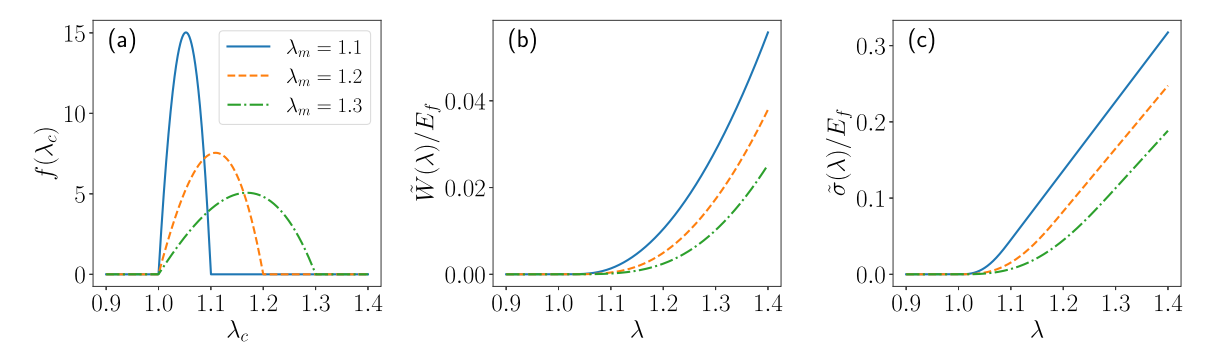


Fig. 10. (a) The quartic recruitment stretch distribution function, $f(\lambda_c)$, given by (A.1). (b) The average fibre segment strain energy density, $\tilde{W}(\lambda)$. (c) The average fibre segment stress, $\tilde{\sigma}(\lambda)$.

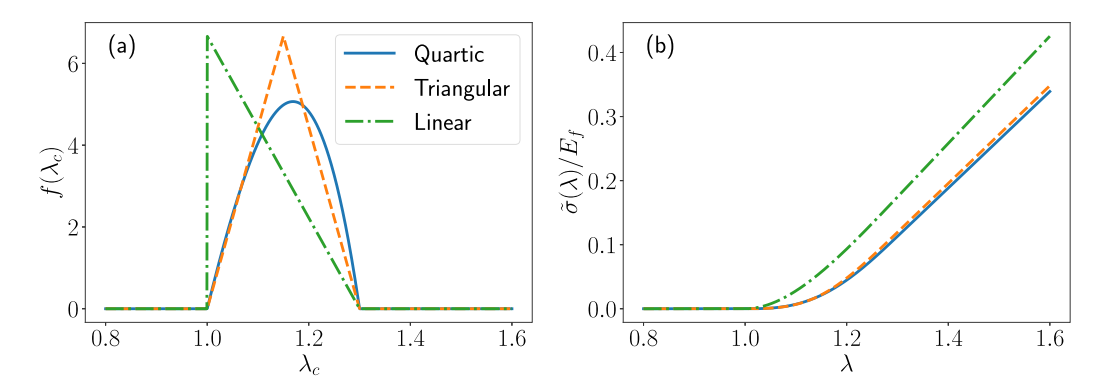


Fig. 11. Comparison of (a) three probability distributions for the fibre recruitment stretches λ_c and (b) the corresponding average fibre segment stress (normalised by the fibre modulus). The fibre distributions and parameter values can be found in Appendix B.

where λ_a denotes the stretch needed to recruit any fibre in the network; λ_* is the mode of the distribution or the most probable stretch that must be exceeded to recruit a fibre; and, as before, λ_m is the maximum stretch that must be exceeded to recruit all fibres in the network. The triangular distribution provides an approximation to the quartic distribution (A.1). The linear distribution is obtained from the triangular distribution (B.1) by taking the limit as $\lambda_* \to 1$ and $\lambda_a \to 1$ to obtain

$$f(\lambda_c) = \begin{cases} 0, & \lambda_c < 1, \\ \frac{2(\lambda_m - \lambda_c)}{(\lambda_m - 1)^2}, & 1 \le \lambda_c < \lambda_m, \\ 0 & \lambda_c \ge \lambda_m. \end{cases}$$
(B.2)

The mode of the linear distribution is located at $\lambda_c = 1$. The corresponding mean strain energy and stress of a fibre segment can be computed following the procedure outlined in Appendix A.

To compare the three distributions, we set the maximum recruitment stretch to $\lambda_m=1.3$. In the triangular distribution, we also set $\lambda_a=1$, so that fibres begin to engage immediately after a tension is applied to the material. We also set the mode of the triangular distribution to $\lambda_*=1.15$, which is the average of λ_a and λ_c . The three distribution functions and the corresponding stresses are shown in Fig. 11. Due to the similarities in the quartic and triangular distributions, the resulting fibre segment stresses are nearly identical. The stress from the linear distribution increases more rapidly with stretch due to this distribution having a smaller mode, implying that less deformation is required on average to engage a fibre. Importantly, when the linear distribution is used, the stress–stretch curve becomes more linear as the stretch increases from one and the 'J' shape of the curve that is present from the quartic and triangular distributions is lost. From these results, we can conclude that the statistical properties of the recruitment distribution, such as the mode and maximum recruitment stretch, control the mechanics of the fibre network rather than the specific functional form of the fibre distribution function.

Appendix C. Elastic energy and stress of equi-biaxial in-plane deformations

We assume the material is subject to an equi-biaxial deformation in the plane of isotropy (i.e. the plane of the fibre network). Thus, the total deformation gradient tensor has the form $\mathbf{F}_t = \operatorname{diag}(\lambda_\parallel, \lambda_\parallel, \lambda_\perp)$, where λ_\parallel and λ_\perp represent the in-plane and out-of-plane stretches, respectively. The elastic component of the Cauchy stress tensor will have the representation $\sigma^e = \operatorname{diag}(\sigma^e_{\parallel}, \sigma^e_{\parallel}, \sigma^e_{\parallel})$.

When the principal stretches of the fibre network are equal, $\lambda_1 = \lambda_2 = \lambda_{\parallel}$, the strain energy functions associated with the fibres, as given in Eqs. (9) and (15), simplify to

$$W_{f} = \frac{E_{f}}{2} (\lambda_{\parallel} - 1)^{2} \quad \text{and} \quad W_{f} = \begin{cases} 0, & \lambda_{\parallel} \leq 1, \\ \frac{E_{f} (\lambda_{\parallel} - 1)^{4} (5\lambda_{m} - 3 - 2\lambda_{\parallel})}{2(\lambda_{m} - 1)^{3} (3 + 4\lambda_{m} + 3\lambda_{m}^{2})}, & 1 \leq \lambda_{\parallel} \leq \lambda_{m}, \\ \frac{E_{f}}{2} + \frac{5E_{f} \lambda_{\parallel} (\lambda_{\parallel} - \lambda_{m} - 1)}{(3 + 4\lambda_{m} + 3\lambda_{m}^{2})}, & \lambda_{\parallel} \geq \lambda_{m}, \end{cases}$$
(C.1)

respectively. The in-plane elastic Cauchy stresses, $\sigma_{\parallel}^e = (\lambda_{\parallel} \lambda_{\perp})^{-1} \partial W_e / \partial \lambda_{\parallel}$, are

$$\sigma_{\parallel}^{e}(\lambda_{\parallel}, \lambda_{\perp}) = (1 - \boldsymbol{\Phi}_{f})\sigma_{\text{NH}} + \frac{\boldsymbol{\Phi}_{f}E_{f}}{2\lambda_{\parallel}\lambda_{\perp}}(\lambda_{\parallel} - 1) \tag{C.2}$$

and

$$\sigma_{\parallel}^{e}(\lambda_{\parallel}, \lambda_{\perp}) = (1 - \boldsymbol{\Phi}_{f})\sigma_{\text{NH}} + \begin{cases} 0, & \lambda_{\parallel} \leq 1, \\ \frac{\boldsymbol{\Phi}_{f}}{\lambda_{\parallel} \lambda_{\perp}} \frac{5E_{f}(\lambda_{\parallel} - 1)^{3}(1 - 2\lambda_{m} + \lambda_{\parallel})}{2(\lambda_{m} - 1)^{3}(3 + 4\lambda_{m} + 3\lambda_{m}^{2})}, & 1 \leq \lambda_{\parallel} \leq \lambda_{m}, \\ \frac{\boldsymbol{\Phi}_{f}}{\lambda_{\parallel} \lambda_{\perp}} \frac{5E_{f}(2\lambda_{\parallel} - 1 - \lambda_{m})}{2(3 + 4\lambda_{m} + 3\lambda_{m}^{2})}, & \lambda_{\parallel} \geq \lambda_{m}, \end{cases}$$
(C.3)

respectively, where

$$\sigma_{\text{NH}}(\lambda_{\parallel}, \lambda_{\perp}) = \frac{E_m}{2(1 + \nu_m)} \frac{1}{\lambda_{\perp}} \left(1 - \frac{1}{\lambda_{\parallel}^2} \right) + \frac{E_m \nu_m}{(1 + \nu_m)(1 - 2\nu_m)} (\lambda_{\parallel}^2 \lambda_{\perp} - 1)$$
(C.4)

is the stress associated with the neo-Hookean matrix. In both cases, the out-of-plane elastic stress, $\sigma_1^e = \lambda_0^{-2} \partial W_e / \partial \lambda_\perp$, is

$$\sigma_{\perp}^{e}(\lambda_{\parallel}, \lambda_{\perp}) = \frac{(1 - \boldsymbol{\Phi}_{f})E_{m}}{1 + \nu_{m}} \left(\frac{1}{2\lambda_{\parallel}^{2}} \left(\lambda_{\perp} - \frac{1}{\lambda_{\perp}} \right) + \frac{\nu_{m}}{(1 - 2\nu_{m})} (\lambda_{\parallel}^{2} \lambda_{\perp} - 1) \right). \tag{C.5}$$

Appendix D. Supplementary data

Supplementary material related to this article can be found online at https://doi.org/10.1016/j.jmps.2025.106350.

Data availability

Data will be made available on request.

References

Agarwal, S., Green, S.I., Phani, A.S., 2023. On the tensile response of formed fiber networks with low areal density. Mech. Res. Commun. 130, 104128.

Agrawal, A., Rahbar, N., Calvert, P.D., 2013. Strong fiber-reinforced hydrogel. Acta Biomater. 9 (2), 5313-5318.

Amajuoyi, J.N., Ilomuanya, M.O., Oseni, B., Azubuike, C.P., Krestou, A., Vorp, D.A., Tsamis, A., Adeosun, S.O., 2024. Scanning electron microscopy-based quantification of keratin and hyaluronic acid microstructure in electrospun scaffolds. Beni Suef Univ. J. Basic Appl. Sci. 13 (1), 77.

Arzash, S., Shivers, J.L., MacKintosh, F.C., 2020. Finite size effects in critical fiber networks. Soft. Matter. 16 (29), 6784-6793.

Åström, J., Saarinen, S., Niskanen, K., Kurkijärvi, J., 1994. Microscopic mechanics of fiber networks. J. Appl. Phys. 75 (5), 2383–2392.

Ateshian, G.A., 2006. Anisotropy of fibrous tissues in relation to the distribution of tensed and buckled fibers. J. Biomech. Eng. 129 (2), 240–249. http://dx.doi.org/10.1115/1.2486179, [Online]. Available.

Ateshian, G.A., Rajan, V., Chahine, N.O., Canal, C.E., Hung, C.T., 2009. Modeling the matrix of articular cartilage using a continuous fiber angular distribution predicts many observed phenomena. J. Biomech. Eng. 131 (6), 061003. http://dx.doi.org/10.1115/1.3118773, [Online]. Available.

Bas, O., De-Juan-Pardo, E.M., Chhaya, M.P., Wunner, F.M., Jeon, J.E., Klein, T.J., Hutmacher, D.W., 2015. Enhancing structural integrity of hydrogels by using highly organised melt electrospun fibre constructs. Eur. Polym. J. 72, 451–463.

Beckett, L.E., Lewis, J.T., Tonge, T.K., Korley, L.T., 2020. Enhancement of the mechanical properties of hydrogels with continuous fibrous reinforcement. ACS Biomater. Sci. Eng. 6 (10), 5453–5473.

Beckett, L.E., Lewis, J.T., Tonge, T.K., Korley, L.T., 2024. Predicting the tensile and compressive modulus of electrospun fiber mat-reinforced hydrogels using the Halpin–Tsai equations. J. Appl. Polym. Sci. 141 (21), e55415.

Bosnjak, N., Wang, S., Han, D., Lee, H., Chester, S.A., 2019. Modeling of fiber-reinforced polymeric gels. Mech. Res. Commun. 96, 7-18.

Castilho, M., Mouser, V., Chen, M., Malda, J., Ito, K., 2019. Bi-layered micro-fibre reinforced hydrogels for articular cartilage regeneration. Acta Biomater. 95, 297-306.

ChemicalBook, 2025. Gelatin. (Accessed 13 February 2025). https://www.chemicalbook.com/ChemicalProductProperty_EN_CB9680379.htm.

Chen, M., Kimpton, L., Whiteley, J., Castilho, M., Malda, J., Please, C., Waters, S., Byrne, H., 2020. Multiscale modelling and homogenisation of fibre-reinforced hydrogels for tissue engineering. European J. Appl. Math. 31 (1), 143–171.

Chen, Z., Lou, R., Zhong, D., Xiao, R., Qu, S., Yang, W., 2021. An anisotropic constitutive model for 3D printed hydrogel-fiber composites. J. Mech. Phys. Solids 156, 104611.

Chen, Y., Zhang, Y., Li, H., Shen, J., Zhang, F., He, J., Lin, J., Wang, B., Niu, S., Han, Z., et al., 2023. Bioinspired hydrogel actuator for soft robotics: Opportunity and challenges. Nano Today 49, 101764.

Chester, S.A., Anand, L., 2010. A coupled theory of fluid permeation and large deformations for elastomeric materials. J. Mech. Phys. Solids 58 (11), 1879–1906. Cox, H.L., 1952. The elasticity and strength of paper and other fibrous materials. Br. J. Appl. Phys. 3 (3), 72.

Davidson, C.D., Jayco, D.K.P., Wang, W.Y., Shikanov, A., Baker, B.M., 2020. Fiber crimp confers matrix mechanical nonlinearity, regulates endothelial cell mechanosensing, and promotes microvascular network formation. J. Biomech. Eng. 142 (11), 111009.

Doi, M., 1996. Introduction to Polymer Physics. Oxford University Press.

Dragan, E.S., 2014. Design and applications of interpenetrating polymer network hydrogels. a review. Chem. Eng. J. 243, 572-590.

Federico, S., 2015. Porous materials with statistically oriented reinforcing fibres. Nonlinear Mech. Soft Fibrous Mater. 49-120.

Federico, S., Gasser, T.C., 2010. Nonlinear elasticity of biological tissues with statistical fibre orientation. J. R. Soc. Interface 7 (47), 955-966.

Federico, S., Grillo, A., 2012. Elasticity and permeability of porous fibre-reinforced materials under large deformations. Mech. Mater. 44, 58-71.

Federico, S., Herzog, W., 2008a. On the anisotropy and inhomogeneity of permeability in articular cartilage. Biomech. Model. Mechanobiol. 7, 367-378.

Federico, S., Herzog, W., 2008b. On the permeability of fibre-reinforced porous materials. Int. J. Solids Struct. 45 (7-8), 2160-2172.

Fuchs, S., Shariati, K., Ma, M., 2020. Specialty tough hydrogels and their biomedical applications. Adv. Heal. Mater. 9 (2), 1901396.

Gasser, T.C., Ogden, R.W., Holzapfel, G.A., 2006. Hyperelastic modelling of arterial layers with distributed collagen fibre orientations. J. R. Soc. Interface 3 (6), 15–35.

Gloria, A., Causa, F., De Santis, R., Netti, P.A., Ambrosio, L., 2007. Dynamic-mechanical properties of a novel composite intervertebral disc prosthesis. J. Mater. Sci., Mater. Med. 18, 2159–2165.

Gregory, J., Hazel, A.L., Shearer, T., 2021. A microstructural model of tendon failure. J. Mech. Behav. Biomed. Mater. 122, 104665.

Grillo, A., Wittum, G., Tomic, A., Federico, S., 2015. Remodelling in statistically oriented fibre-reinforced materials and biological tissues. Math. Mech. Solids 20 (9), 1107–1129.

Halpin, J., Kardos, J., 1976. The Halpin-Tsai equations: a review. Polym. Eng. Sci. 16 (5), 344-352.

Hamedzadeh, A., Gasser, T.C., Federico, S., 2018. On the constitutive modelling of recruitment and damage of collagen fibres in soft biological tissues. Eur. J. Mech. A Solids 72, 483–496.

Haraguchi, K., Takehisa, T., 2002. Nanocomposite hydrogels: A unique organic-inorganic network structure with extraordinary mechanical, optical, and swelling/de-swelling properties. Adv. Mater. 14 (16), 1120–1124.

Hashlamoun, K., Grillo, A., Federico, S., 2016. Efficient evaluation of the material response of tissues reinforced by statistically oriented fibres. Z. Für Angew. Math. Phys. 67 (5), 113.

Haughton, J., Cotter, S.L., Parnell, W.J., Shearer, T., 2022. Bayesian inference on a microstructural, hyperelastic model of tendon deformation. J. R. Soc. Interface 19 (190), 20220031.

Head, D., Levine, A., MacKintosh, F., 2003. Distinct regimes of elastic response and deformation modes of cross-linked cytoskeletal and semiflexible polymer networks. Phys. Rev. E 68 (6), 061907.

Holmes, M., Mow, V.C., 1990. The nonlinear characteristics of soft gels and hydrated connective tissues in ultrafiltration. J. Biomech. 23 (11), 1145–1156. Holzapfel, G.A., Ogden, R.W., 2010. Constitutive modelling of arteries. Proc. R. Soc. A 466 (2118), 1551–1597.

Hong, W., Zhao, X., Zhou, J., Suo, Z., 2008. A theory of coupled diffusion and large deformation in polymeric gels. J. Mech. Phys. Solids 56 (5), 1779–1793.

Humphries, D., Grogan, J., Gaffney, E., 2018. The mechanics of phantom Mikado networks. J. Phys. Commun. 2 (5), 055015.

Ishihara, K., Shi, X., Fukazawa, K., Yamaoka, T., Yao, G., Wu, J.Y., 2023. Biomimetic-engineered silicone hydrogel contact lens materials. ACS Appl. Bio. Mater. 6 (9), 3600–3616.

Jordan, A.M., Kim, S.-E., Van de Voorde, K., Pokorski, J.K., Korley, L.T., 2017. In situ fabrication of fiber reinforced three-dimensional hydrogel tissue engineering scaffolds. ACS Biomater. Sci. Eng. 3 (8), 1869–1879.

Klarbring, A., Torstenfelt, B., Hansbo, P., Larson, M.G., 2017. Optimal design of fibre reinforced membrane structures. Struct. Multidiscip. Optim. 56, 781–789. Lanir, Y., 1983. Constitutive equations for fibrous connective tissues. J. Biomech. 16 (1), 1–12.

Li, J., Östling, M., 2013. Percolation thresholds of two-dimensional continuum systems of rectangles. Phys. Rev. E 88 (1), 012101.

Li, J., Zhang, S.-L., 2009. Finite-size scaling in stick percolation. Phys. Rev. E 80 (4), 040104.

Moore, A.C., Hennessy, M.G., Nogueira, L.P., Franks, S.J., Taffetani, M., Seong, H., Kang, Y.K., Tan, W.S., Miklosic, G., El Laham, R., et al., 2023. Fiber reinforced hydrated networks recapitulate the poroelastic mechanics of articular cartilage. Acta Biomater. 167, 69–82.

Nasra, S., Patel, M., Shukla, H., Bhatt, M., Kumar, A., 2023. Functional hydrogel-based wound dressings: A review on biocompatibility and therapeutic efficacy. Life Sci. 334, 122232.

Nian, X., Yang, Q., Rao, W., 2023. Constitutive modeling for hydrogel composites with arbitrary fiber distribution. Compos. Struct. 321, 117283.

Niskanen, K., Alava, M.J., 1994. Planar random networks with flexible fibers. Phys. Rev. Lett. 73 (25), 3475.

Ogden, R.W., 2015. Nonlinear elasticity with application to soft fibre-reinforced materials. In: Nonlinear Mechanics of Soft Fibrous Materials. Springer, pp. 1–48. Paetsch, C., Trimmer, B., Dorfmann, A., 2012. A constitutive model for active-passive transition of muscle fibers. Int. J. Non-Linear Mech. 47 (2), 377–387.

Park, S., Krishnan, R., Nicoll, S.B., Ateshian, G.A., 2003. Cartilage interstitial fluid load support in unconfined compression. J. Biomech. 36 (12), 1785-1796.

Räisänen, V., Alava, M., Niskanen, K., Nieminen, R., 1997. Does the shear-lag model apply to random fiber networks? J. Mater. Res. 12 (10), 2725–2732. Revete, A., Aparicio, A., Cisterna, B.A., Revete, J., Luis, L., Ibarra, E., Segura González, E.A., Molino, J., Reginensi, D., 2022. Advancements in the use of

hydrogels for regenerative medicine: properties and biomedical applications. Int. J. Biomater. 2022 (1), 3606765.
Safavi, H.R., Amiri, A., Baniassadi, M., Zolfagharian, A., Baghani, M., 2023. An anisotropic constitutive model for fiber reinforced salt-sensitive hydrogels. Mech.

Safavi, H.R., Amiri, A., Baniassadi, M., Zolfagharian, A., Baghani, M., 2023. An anisotropic constitutive model for fiber reinforced saft-sensitive hydrogels. Mech. Adv. Mater. Struct. 30 (23), 4814–4827.

Sakai, T., Matsunaga, T., Yamamoto, Y., Ito, C., Yoshida, R., Suzuki, S., Sasaki, N., Shibayama, M., Chung, U.-i., 2008. Design and fabrication of a high-strength hydrogel with ideally homogeneous network structure from tetrahedron-like macromonomers. Macromol. 41 (14), 5379–5384.

Schwartz, L.M., Feng, S., Thorpe, M., Sen, P.N., 1985. Behavior of depleted elastic networks: Comparison of effective-medium and numerical calculations. Phys. Rev. B 32 (7), 4607.

Shearer, T., 2015a. A new strain energy function for modelling ligaments and tendons whose fascicles have a helical arrangement of fibrils. J. Biomech. 48 (12), 3017–3025.

Shearer, T., 2015b. A new strain energy function for the hyperelastic modelling of ligaments and tendons based on fascicle microstructure. J. Biomech. 48 (2), 290–297.

Shearer, T., Parnell, W.J., Lynch, B., Screen, H.R., David Abrahams, I., 2020. A recruitment model of tendon viscoelasticity that incorporates fibril creep and explains strain-dependent relaxation. J. Biomech. Eng. 142 (7), 071003.

Shivers, J.L., Arzash, S., Sharma, A., MacKintosh, F.C., 2019. Scaling theory for mechanical critical behavior in fiber networks. Phys. Rev. Lett. 122 (18), 188003. Smith, A.M., Senior, J.J., 2021. Alginate hydrogels with tuneable properties. Tunable Hydrogels Smart Mater. Biomed. Appl. 37–61.

Stella, J.A., Wagner, W.R., Sacks, M.S., 2010. Scale-dependent fiber kinematics of elastomeric electrospun scaffolds for soft tissue engineering. J. Biomed. Mater. Res. Part A 93 (3), 1032–1042.

Strange, D.G., Tonsomboon, K., Oyen, M.L., 2014. Mechanical behaviour of electrospun fibre-reinforced hydrogels. J. Mater. Sci., Mater. Med. 25, 681–690.

Tan, W.S., Moore, A.C., Stevens, M.M., 2023. Minimum design requirements for a poroelastic mimic of articular cartilage. J. Mech. Behav. Biomed. Mater. 137, 105528.

Trefethen, L.N., Weideman, J., 2014. The exponentially convergent trapezoidal rule. SIAM Rev. 56 (3), 385–458.

Vainio, A., Paulapuro, H., 2005. Observations on interfibre bonding and fibre segment activation based on the strength properties of laboratory sheets. Nord. Pulp Pap. Res. J. 20 (3), 340–344.

Vainio, A., Paulapuro, H., 2007. Interfiber bonding and fiber segment activation in paper. BioResour. 2 (3), 442-458.

Vasta, M., Gizzi, A., Pandolfi, A., 2018. A spectral decomposition approach for the mechanical statistical characterization of distributed fiber-reinforced tissues. Int. J. Non-Linear Mech. 106, 258–265.

Visser, J., Melchels, F.P., Jeon, J.E., Van Bussel, E.M., Kimpton, L.S., Byrne, H.M., Dhert, W.J., Dalton, P.D., Hutmacher, D.W., Malda, J., 2015. Reinforcement of hydrogels using three-dimensionally printed microfibres. Nat. Commun. 6 (1), 1–10.

Zhang, X., Jiang, Y., Han, L., Lu, X., 2021. Biodegradable polymer hydrogel-based tissue adhesives: A review. Biosurface Biotribology 7 (4), 163-179.